ABSTRACT

AL-TAWHID, ATHBY HUMOUD. Controlling the Emergent Phenomena at Polar/Nonpolar Interfaces by Molecular Beam Epitaxy. (Under the direction of Dr. Divine Kumah).

Complex oxide perovskite materials are a family of materials with a variety of interesting properties such as high temperature superconductivity, Colossal magnetoresistance and multiferroicity. At the interface of oxide perovskites, exciting emergent phenomena can occur which are not found in either of their bulk constituents such as the formation of a 2-dimensional electron gas (2-deg), ferromagnetism and superconductivity. Understanding the mechanisms which lead to the appearance of these interesting phenomena as well controlling their formation is an important step in utilizing these interfaces in new device applications.

In this thesis, we study the interface between $LaCrO_3/SrTiO_3$ (LCO/STO) which was originally found to be insulating. By tuning the growth parameters, we were able to facilitate the formation of a high mobility (2-deg). We study the difference between the insulating and metallic interface using a variety of methods which include Angle resolved Photoemission Spectroscopy (ARPES), Electronic transport using a physical properties measurement system (PPMS) and high-resolution synchrotron X-ray diffraction. We compare the structural and electronic properties of the material and elucidate the mechanisms which lead to the formation of the 2-deg.

We also study the interface between $LaCrO_3/LaMnO_3$ superlattice grown on STO. We find that LCO/LMO superlattice is ferrimagnetic with a Neal temperature of 150K. The formation of a high mobility 2-deg is suppressed despite the polar nature of LCO and LMO. We attribute the lack of conductivity at the interface to the trapping and accumulation of charge in the LMO layers as evidence by the large percent of Mn^{+2} in our XMCD results.

Controlling the Emergent Phenomenon at The Polar/Non-Polar $LaCrO_3/SrTiO_3$ Interface by Tuning Growth Parameters.

by
Athby Humoud Al-Tawhid

A dissertation submitted to the Graduate Faculty of
North Carolina State University
in partial fulfillment of the
requirements for the degree of
Doctor of Philosophy

Physics

Raleigh, North Carolina
2019

APPROVED BY:

_____	_____
Divine P. Kumah Committee Chair	Dali Sun
_____	_____
Daniel Dougherty	Douglas Irving

DEDICATION

I dedicate this thesis to anyone that loves me enough to read it.

BIOGRAPHY

Athby Al-Tawhid was born in Kuwait City, Kuwait on June 22nd, 1990. He received his Bachelor of Science in physics from the University of North Carolina Asheville in 2012. He joined North Carolina State University in 2014 as a physics graduate student after taking a year off. He joined Divine Kumah's group in 2016 and will hopefully graduate in 2020 if all goes well.

ACKNOWLEDGMENTS

I'd like to acknowledge all those who have helped me during my PhD. First my loving wife and fellow physicist. She has always been there to support me in all my endeavors and has made even the most grueling of weeks amazing with her loving presence.

I'd also like to acknowledge my PhD advisor Divine Kumah. It is from him that I acquired most of my skills and knowledge. He has been a mentor to me and has helped me grow both as a scientist and a person. His kindness and passion are two of his traits that I admire the most and I wish to emulate in myself. Without him I would obviously not have been able to complete my PhD.

Last, I would like to acknowledge my committee members and group members whose conversations have helped shape my PhD and thesis.

TABLE OF CONTENTS

LIST OF TABLES

LIST OF FIGURES

CHAPTER 1

Introduction

1.1 Complex Oxides and Interfaces

Complex oxide materials are a family of materials with the ABO_3 chemical formula, where A is typically, but not limited to rare earth metals and B are transition metals. The materials take on a perovskite crystal structure as seen in Figure 1. The crystal structure can be cubic as seen in figure 1.1 with $SrTiO_3$ as the most common example. In many complex oxide materials, the oxygen octahedra tilts and rotates and the cations displace leading to lower symmetry systems such as orthorhombic and rhombohedral crystal structures.

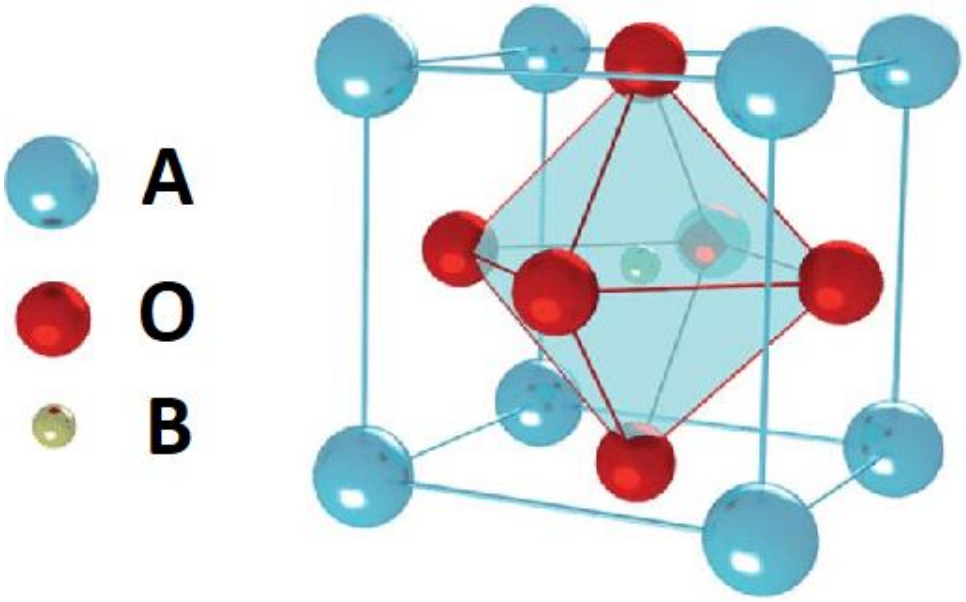

Figure 1.1. Illustration of a cubic perovskite unit cell. A and B are cations which are rare earth and transition metals and the red spheres are oxygens in an octahedra. (Y. Chen) [1]

Complex oxide materials exhibit a wide range of novel and exotic properties such as high temperature superconductivity, colossal magnetoresistance and multiferroicity [2-5]. However, in order to utilize these material's in modern electronic devices, thins films and heterostructures need to be fabricated. At these interfaces, the material's electronic and magnetic states as well as their structure can be quite different from their bulk. In some instance, the result is undesirable, such as the appearance of the magnetic dead layer in LSMO thin film, where LSMO films below a critical thickness lose their magnetic properties [6]. On the other side, at some oxide interfaces, new and exotic properties can emerge such as the appearance of a 2-dimensional electron gas at the interface between $LaAlO_3$ and $SrTiO_3$ which are bulk insulators [7]. Understanding the fundamental physics which occur at these interfaces and harnessing their potential is an ongoing goal in the field of material science.

1.2 Polar Discontinuity

A special class of interfaces are one where one material is polar and the other is not. A polar perovskite material is one where the total charge of each atomic layer alternates along a specific crystallographic direction. A non-polar material is one where the total charge of each layer is neutral. Figure 1.2 shows illustration of $LaAlO_3$ (LAO) grown on $SrTiO_3$ (STO), a polar material grown on a non-polar material. For the LAO, along the 001 direction, the LaO planes have a net charge of +1 e since the La is in the +3 state and the oxygen is -2. On the other hand, the AlO_2 planes have a -1e total charge since the Al is +3 and the two oxygens are in the -2 state each. The material it is grown on STO, is neutral since the SrO planes have a net charge of zero since the Sr is in the +2 state and the oxygen is -2 and the TiO_2 planes also have zero net charge since the Ti is +4 state and the two oxygens are in the -2 state.

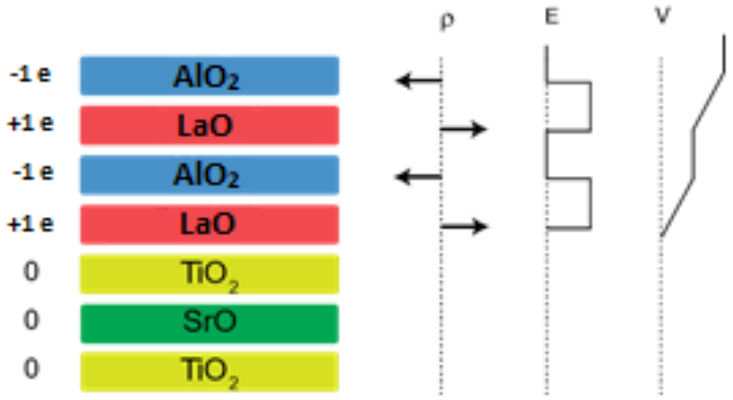

Figure 1.2. Illustration of the interface of a polar material $LaAlO_3$ grown on $SrTiO_3$. The alternating charge stacking creates an electric field in the polar material. The presence of the electric field causes the electric potential to increase with thickness of the polar material. (S. Koofar) [8]

Figure 1.2 also shows the electric field as we move along the 001 direction. The electric potential which is the integral of the electric field increase monotonically as we move along the 001 direction. The result is that the electric potential increases with the thickness of the polar material and diverges with layer thickness. This is energetically unfavorable, and the material will have to do something to alleviate the polar discontinuity.

1.3 Mechanisms to alleviate the polar discontinuity

The first mechanism we will discuss is electronic charge transfer. In this mechanism, as the electric potential increases with increasing thickness, there will be a critical thickness where it will be energetically favorable for half an electron to transfer from the topmost layer of the polar material to the interface. The resulting charge redistribution will lead to the electric field

zigzagging as seen in figure 1.3, and the electric potential no longer diverges with thickness. An interesting consequence of charge transfer is that the electronic state at the interface will differ from the bulk due to the extra charge there. These charges can be localized as is the case for $LaMnO_3$/STO. In this case, the charge is transferred to the LMO side of the interface and changes the Mn oxidation state from +3 to +2. This results in ferromagnetism which appears after a critical thickness of LMO is grown on STO[9].

In some systems, like LAO/STO, the charges are iterant, and the result is that a 2-dimensional gas (2-deg) is formed at the STO side of the interface [7]. This 2-deg exhibits interesting properties such high mobility and even superconductivity at low temperature [10]. There are even some reports of weak ferromagnetism which persist up to room temperature[11].

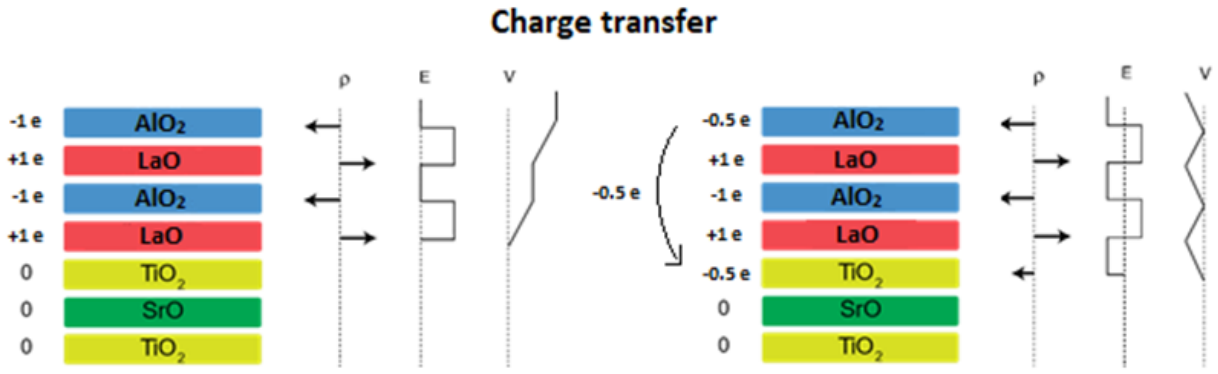

Figure 1.3. (Left) Illustration of the interface of a polar material $LaAlO_3$ grown on $SrTiO_3$ showing the electric field and electric potential which diverges. (Right) half an electron from the top layer of the polar material transfers to the top of the STO. The resulting charge redistribution alters the electric field in the manner shown and the electric potential no longer diverges. (S. Koofar) [8]

The second mechanism which can alleviate the polar discontinuity is the formation of polar distortions in the polar material [12]. In this scenario, the AO and BO_2 planes which have a total charge of 1 and -1 respectively, buckle and deform as seen in figure 1.4. The result is that an electric dipole forms which creates an electric field which counteracts the divergence of the electric potential. This buckling leads to an increase in the bond angle of the cation and oxygen anion and can alter the bandwidth of the electronic states of the cations. In some cases, this can lead to altering the properties of the polar material. An example of this would be growing thin films of $La_{0.7}Sr_{0.3}MnO_3$ on STO. For thin films, the buckling is thought to be one of the reasons why its magnetic properties are suppressed [13].

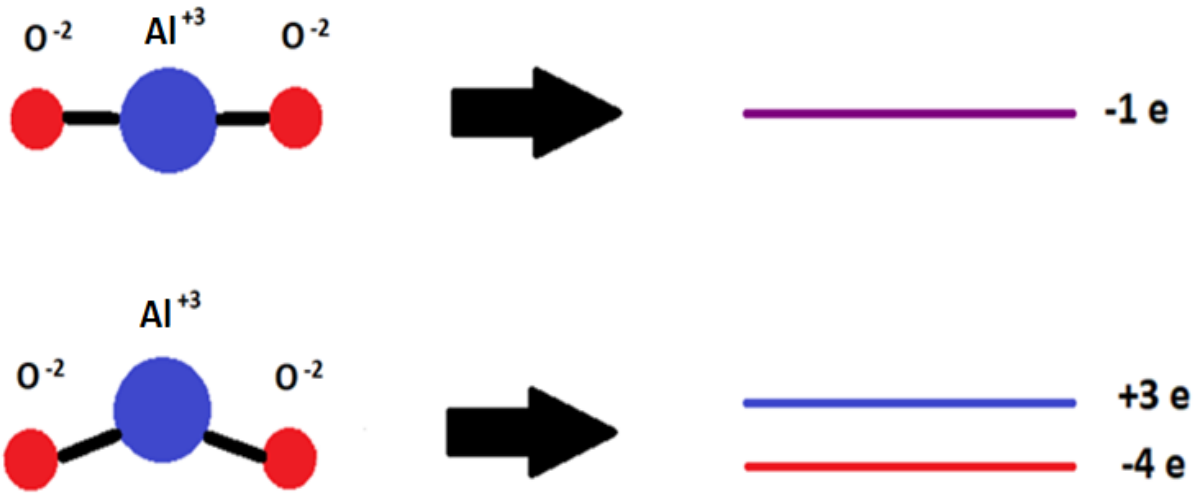

Figure 1.4. The BO_2 of LAO which has a formal charge of -1e when the bond angle between the cation and oxygen is 180 degrees. Polar distortion in the form of a buckling of the layer with the oxygen moving down relative to the cation. This can be modeled as two layers with charge of +3e and -4e with the distance between the layers equal to the magnitude of the displacement of the oxygen atoms.

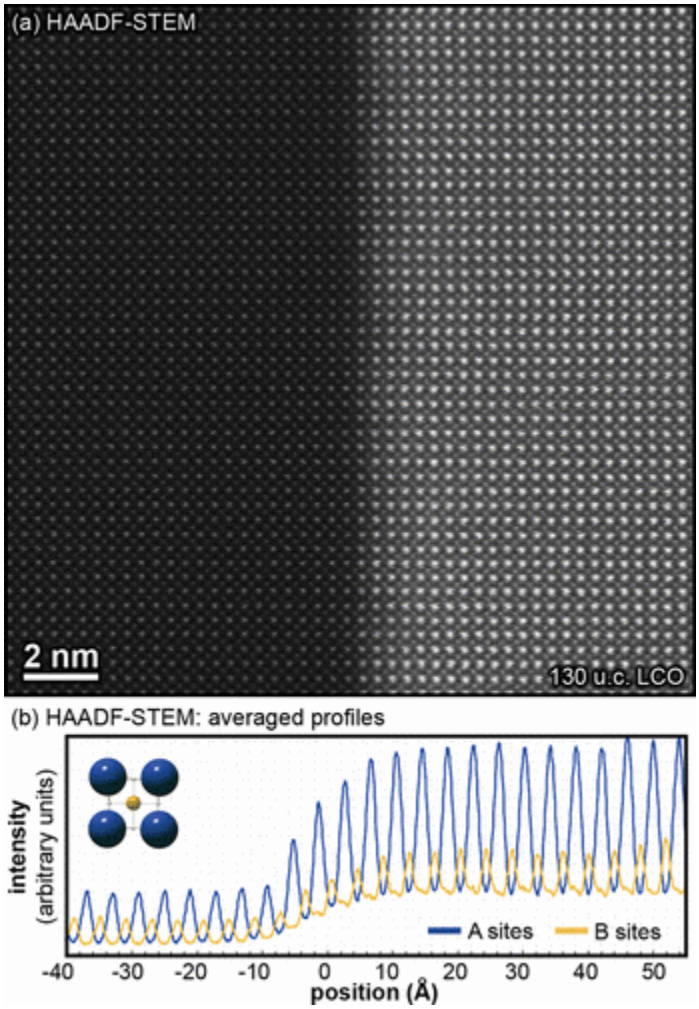

Figure 1.5. (a) A cross-sectional HAADF-STEM image of 130-u.c. LCO/STO heterostructure, (b) Averaged intensity of the HAADF images over 0.8- Å wide lines across the interface for the A-site and B sites. You can clearly see that the intensity gradually changes over the course of 20 Å (5-unit cells) (R. Colby) [14]

The last mechanism which I will discuss is that of cation intermixing. In the fig 1.2 the interface between the polar material and non-polar substrate is chemically abrupt. In reality, interfaces are rarely this abrupt and instead a gradual change from one chemical species to the

other occurs over a few unit cells. Fig 1.5[14] shows a aigh-angle annular dark-field scanning transmission electron microscopy (HAADF-STEM) image of the interface between LCO/STO. Examining the intensity of the A and B site columns across the interfaces shows that intermixing of the cations occurs over 4-5-unit cells. This leads to a more gradual change in the charge stacking of the atomic planes which leads to a reduction of the electrostatic potential. This chemical doping could also be responsible for the formation of mobile charges at the interfaces [15].

1.4 2-Diminsional electron gas at complex oxide interfaces

The discovery of a 2-deg at the interface of two complex oxide materials was made in 2004 by Ohtomo and Hwang between band insulators $LaAlO_3$ and $SrTiO_3$[7]. While the formation of a 2-deg has been previously discovered in other material systems such as III-V conventual semiconductors and binary oxides[16,17], the discovery generated an immense amount of interest from the scientific community. Complex oxides are a class of materials were the electronic, lattice and spin degree of freedom are coupled the electron-electron interactions are quite strong. Since then there have thousands of publications on the formation of 2-degs at LAO/STO and many other perovskites interfaces[18-21].

One of the open questions regarding the formation of 2-degs at oxide interfaces, was the origin of the mobile carriers. Some authors were proponents of the polar catastrophe model, where charge transfer occurs from the surface of the polar materials was due solely from electrostatic considerations[22]. Others suggested that the origin was due to trapping of the oxygen vacancies on the STO side of the interface during the growth process[23]. Some thought that origin was due to chemical doping due to intermixing at the interface[15]. There was no consensus at the time, and the topic is still under debate to this day[24].

There is a lot of experimental work that has been done on oxide interfaces. It was shown that the formation of the 2-deg required a minimum thickness of the polar material which suggested the polar catastrophe model was accurate[7,21]. It was also shown that the growth conditions in the form of temperature, oxygen pressure and cation stoichiometry played an important role in whether the interface was conducting or not[23]. This strongly suggest that the polar catastrophe model alone is not enough to explain all the experimental data to date.

Another open question at the time was the dimensionality of the 2-deg. Hall measurements put the sheet carrier density of the 2-deg at the LAO/STO interface between 10^{17} and 10^{13} cm^{-2} depending on the growth conditions and post growth annealing[7,23]. Several methods were used to determine the thickness of the conducting layer. One of the first came from analyzing the Shubnikov de Haas (SdH) oscillations in magnetoresistance measurements. For samples with sheet carrier concentrations of 10^{17} cm^{-2}, the analysis of the period of the oscillations of the SdH put the thickness of the conducting layer in excess of a hundred micron[25]. For samples with lower sheet carrier concentration, the mobilities were lower and SdH oscillations could not be observed. These results show that 3D conduction can occur depending on the growth conditions[25].

A more direct method to measure the dimensionality of the conducting layer that was utilized was with a conducting tip atomic force microscopy (CT-AFM). Here several samples of LAO/STO interfaces with varying growth condition and annealing and subsequently carrier concentration were studied. Both samples were grown by PLD with a growth temperature of 750 ^{o}C and partial oxygen pressure of 10^{-5} and 10^{-6} mbar respectively. The latter sample was cooled in 300 mbar of O_2 to fill any oxygen vacancies in the STO. Figure 1.6 a) and c) shows their measured sheet carrier concentrations at room temperature and 4K and their sheet resistance vs temperature[26].

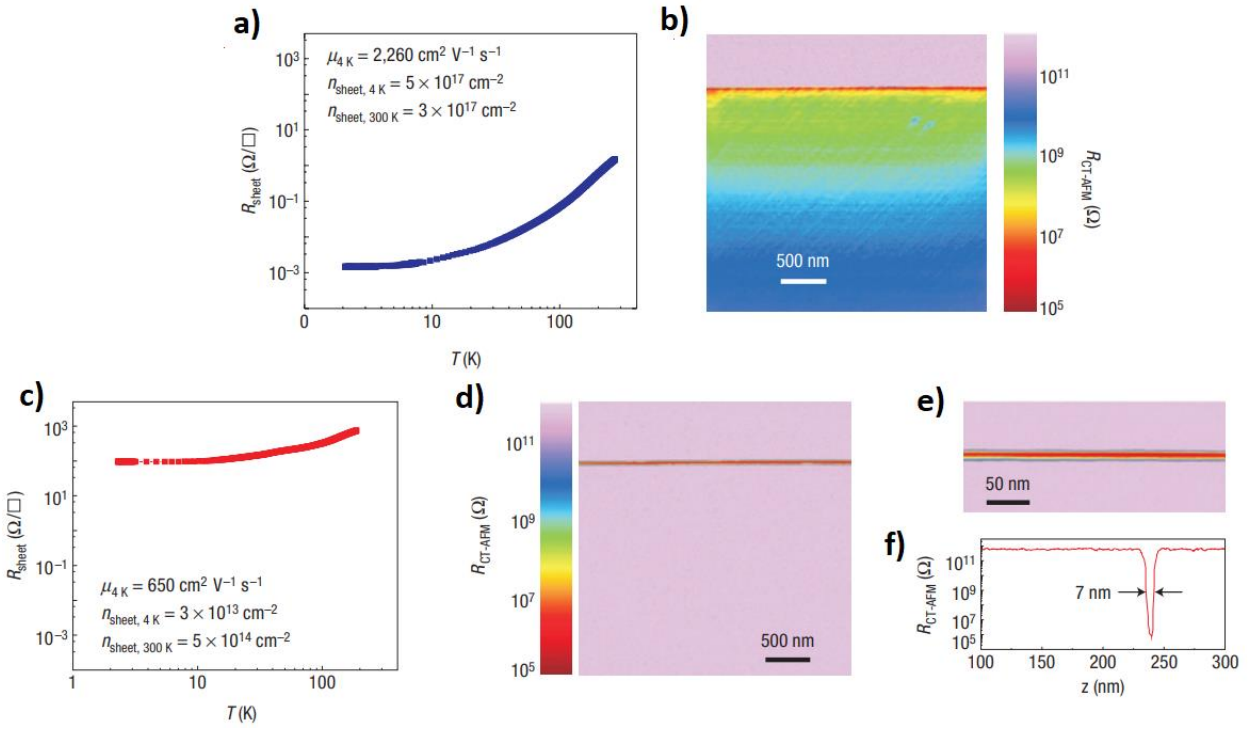

Figure 1.6 (a) Sheet resistance vs temperature for unannealed LAO/STO. b) CT-AFM resistance mapping around the interface of the unannealed LAO/STO. c) Sheet resistance vs temperature for annealed LAO/STO. d) CT-AFM resistance mapping around the interface of annealed LAO/STO e) Higher resolution CT-AFM resistance mapping around the interface of annealed LAO/STO f) Profile of the measured CT resistance across the interface of the annealed LAO/STO. (M. Basletic) [26]

For the unannealed sample the CT-AFM image in figure 1.6 b) shows that the conducting layer extends very deep into the STO layer. However, for the annealed sample the c-AFM in figure d) & e) shows that the conducting layer is confined to the interface and is 7nm thick. The thickness of the conducting tip and the uncertainty in the lateral motion of the tip means that this is likely an overestimate and we can use it as an upper limit on the thickness. The results from this study reveal that the thickness of the conducting layer is highly dependent on the growth conditions of the films.

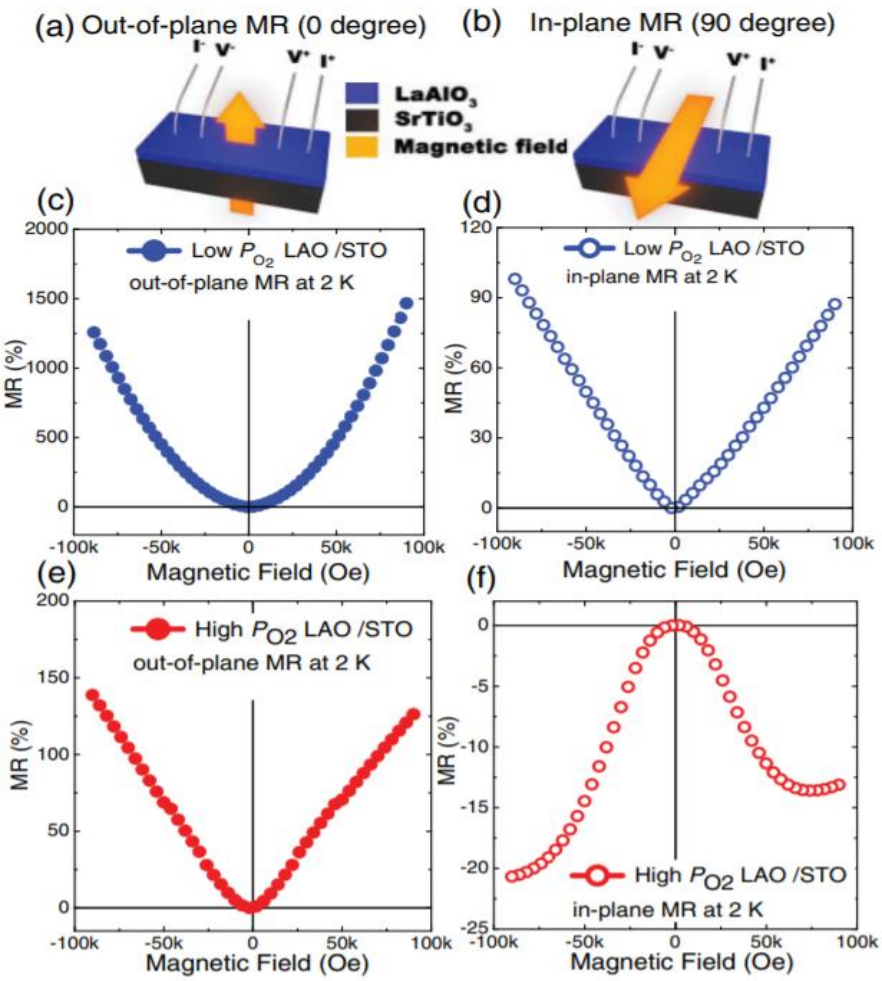

Figure 1.7. Comparison on magnetoresistance between high PO_2 and low PO_2 with magnetic field applied at different directions. Illustration for an (a) out-of-plane and (b) in-plane linear measurement geometry. (c) Low-PO_2 $LaAlO_3/SrTiO_3$ interfaces out-of-plane MR. (d) Low-PO_2 $LaAlO_3/SrTiO_3$ interface in-plane MR. (e) High-PO_2 interfaces out-of-plane MR. (f) High-PO_2 interfaces in-plane MR. (X. Wang)[27].

Comparing the magnetoresistance (MR) of the samples with 2D and 3D conduction, we find that they possess different MR relationships. X. Wang et al. showed that samples with 2D conduction, as evidenced by their low sheet carrier concentrations ($<10^{14}$ cm^{-2}), possessed negative

MR with the in-plane geometry, while the sample with 3D conduction show a positive MR[27]. The origin of the negative MR was attributed by the author to be due to weak localization or Kondo scattering. Regardless of the origin, this difference acts a very convenient method to distinguish the dimensionality of the conducting layer at the LAO/STO interface.

1.4 2-Diminsional electron gas and the $LaCrO_3/SrTiO_3$ interface

Polar/nonpolar perovskite interfaces have attracted considerable scientific interest since their interfaces can possess unique properties not found in the bulk of either materials. Understanding the mechanisms which lead to the formation of these properties is an important physical question which is necessary if we wish to harness these properties for the purpose of designing new devices. The focus of this thesis will be on the formation of a 2-dimensional gas at the interface of polar/nonpolar perovskite materials. The most studied polar/nonpolar interface in which a 2-deg forms is LAO/STO. Since its discovery, many other perovskite materials have been grown on STO and a 2deg has been shown to form at the interface of many of them. However, not all interfaces form a 2-deg despite the existence of a polar discontinuity between them. Studying these interfaces with closer detail can give valuable insight into the mechanisms that lead to the formation of 2-degs at polar/nonpolar interface. In this thesis, we have chosen to investigate the $LaCrO_3$/STO interface and determine the dominant mechanisms which mitigate the polar discontinuity and the emergent phenomena that follow from these mechanisms.

The LCO/STO heterostructure was first found to be insulating with no 2-deg forming at the interface [28]. It was theorized that the charge transfer was the mechanism that mitigated the polar discontinuity, but that Ti out diffusion into the LCO film resulted in deep trap states which captured the transferred electrons. The result was that charge transfer did occur but was contained

within the LCO film and thus no 2-deg is formed. PLD growth later showed that the interface was conductive [29], but only when the oxygen partial pressure was low enough. It was also shown that LCO/STO superlattices exhibit conductivity [30].

In this thesis, we use molecular beam epitaxy to grow high quality LCO/STO heterostructure. By varying the growth parameters, we can tune the interface from insulating to high mobility 2-dimensional gas. To gain insight into the difference between the two samples we perform synchrotron X-ray diffraction, X-ray and angle resolved photo emission spectroscopy as well as measure their transport and magneto transport properties. We discuss their difference in the mechanisms that alleviate the polar discontinuity and postulate on the methods to further alter and enhance their properties.

1.5 $LaCrO_3/LaMnO_3$ superlattice on $SrTiO_3$

Since the discovery of the 2-dimensional gas at the LAO/STO [7] there have been continued interest in modifying the properties of the 2-deg to create new devices. While some have focused their efforts on improving the mobility and modifying the carrier concentration [31,32], others have attempted to induce new magnetic properties in the 2-deg. The attempts to magnetize the 2-deg have been done by growing different magnetic overlayers on STO in different ways. Some have grown thin magnetic films between LAO and STO [31]. The main issue with this method is that these films need to be very thin for the 2-deg to form(<1uc). Due to the magnetic dead layer, an effect where the magnetic properties of very thin films are suppressed, achieving a magnetic thin film on this scale is quite difficult [13].

Another method is to grow a magnetic polar material on STO directly. An example of this would be $LaMnO_3$ (LMO) grown on STO. Like LAO and LCO, LMO is polar along the 001

direction, so charge transfer and the resulting 2-deg should form at the interface of LMO and STO. However, this interface is insulating, and instead ferromagnetism occurs when a critical thickness of LMO is grown on STO [33]. It is theorized that charge transfer occurs when the LMO exceeds a critical thickness, but that the charge is transferred to the LMO side of the interface resulting in mixture of Mn^{+3} and Mn^{+2}. [34]. While this mechanism does result in ferromagnetism, it suppresses the formation of a 2-deg.

In this thesis, we use MBE to grow a superlattice of LCO/LMO on STO. The goal is to study the charge transfer in this system using a variety of experiments to probe the dominant mechanisms in which the system alleviates the polar discontinuity and the possible resulting emergent phenomena.

REFERENCES

[1] Y. Chen, L. Zhang, Y. Zhang, H. Gao, H. Yan, *RSC Advances,* **2018,** 8(19), pp.10489 10508

[2] J. Mannhart, D. G. Schlom, *Science (80-.).* **2010**, *327*, 1607 LP.

[3] V. J. Emery, *Phys. Rev. Lett.* **1987**, *58*, 2794.

[4] Y. Tokura, Y. Tomioka, H. Kuwahara, A. Asamitsu, Y. Moritomo, M. Kasai, *J. Appl. Phys.* **1996**, *79*, 5288.

[5] H. Liu, X. Yang, *Ferroelectrics* (2017), 507:1, 69-85

[6] Verna, A., et al. *Journal of magnetism and magnetic materials,* **2010,** 322.9-12: 1212-1216.

[7] A. Ohtomo, H. Y. Hwang, *Nature* **2004**, *427*, 423.

[8] S. Koofar, *Phd Thesis*, **2019**, page 2.

[9] Wang, X. Renshaw, et al. *Science,* **2015,** 716-719.

[10] Gariglio, Stefano, et al. *Journal of Physics: Condensed Matter*, **2009**, 164213.

[11] Dikin, D. A., et al. *Physical Review Letters,* **2011**, 107.5, 056802.

[12] R. Pentcheva, W. Pickett. *Physical review letters,* **2009**, 102.10 107602.

[13] S. Koohfar, et al. *Physical Review B,* **2017,** 96.2, 024108.

[14] R. Colby, et al. *Physical Review B,* 2013, 88.15, 155325.

[15] P. Willmott et al., *Phys. Rev. Lett*., **2007,** 99, 155502.

[16] Ipri, A. C. *Applied Physics Letters*, **1973,** 16-18, 22.1.

[17] Meng, Li, et al. *Journal of Nanomaterials* **2015**. 2015, 694234.

[18] Moetakef, Pouya, et al. *Applied Physics Letters,* **2011**, 99.23, 232116.

[19] He, C., et al. *Physical Review B*, **2012**, 86.8, 081401.

[20] Perna, Paolo, et al. *Applied Physics Letters*, **2010**, 97.15, 152111.

[21] Annadi, A., et al. *Physical Review B*, **2012**, 86.8, 085450.

[22] Savoia, A., et al. *Physical Review B*, **2009**, 80.7, 075110.

[23] A. Kalabukhov, R. Gunnarsson, J. Börjesson, E. Olsson, T. Claeson, and D. Winkler, *Phys. Rev. B*, **2007**, 75, 121404.

[24] Gariglio, Stefano, M. Gabay, and J-M. Triscone. *APL Materials*, **2016**, 4.6, 060701.

[25] Herranz, Gervasi, et al. *Physical review letters*, **2007**, 98.21, 216803.

[26] Basletic, M., et al. *Nature materials*, **2008**, 7.8, 621-625.

[27] X. Wang W. Lü, A. Annadi, Z. Liu, K. Gopinadhan, S. Dhar, T. Venkatesan et al., *Phys. Rev. B*, **2011**, 84, 075312.

[28] S. Chambers, et al. *Physical review letters*, **2011**, 107.20, 206802.

[29] L. Cheng-Jian, et al. *Scientific reports*, **2018,** 8.1, 1-11.

[30] Lin, S-C., et al. *Physical Review B*, **2018**, 98.16, 165124.

[31] Chen, Y., Bovet, N., Trier, F. et al. *Nat Commun*, **2013**, 4, 1371.

[32] Chen, Y. Z., et al, *Nature materials*, **2015** 14.8 801-806.

[33] Wang, X. Renshaw, et al. *Science*, **2015** 716-719, 349.6249.

[34] Kaspar, Tiffany C., et al., *Advanced Materials Interfaces*, **2019**, 6.1, 1801428.

CHAPTER 2

Experimental methods

2.1 Growth of Complex Oxides

2.1.1 Molecular Beam Epitaxy (MBE)

There are numerous methods to grow thin film oxide materials such as pulsed laser deposition, direct sputtering and molecular beam epitaxy (MBE). Each of these methods of growth comes with its own set of advantages and disadvantages. In this thesis, we will be using molecular beam epitaxy as our method of growth. MBE growth involves loading the substrate into a vacuum chamber. The base pressure of the chamber is around 10^{-10} torr which significantly reduces the chance of contamination. Source material comprising of very pure single elements are heated individually in high temperature effusion cells. At temperatures that are material specific, the elements begin to sublimate, and an elemental vapor also known as a molecular beam is produced. Shutters are place in the chamber to block the molecular beam until the growth is ready to begin. Prior to growth, the rate of deposition from the effusion cells is calibrated for each element using a quartz crystal microbalance (QCM) to achieve the desired stoichiometry. The substrate is typically heated to some desired temperature to facilitate the growth of the material. Oxygen, either in its molecular form or as a plasma is let into the chamber until a specific pressure is reached (typically $1e^{-9}$-$1e^{-5}$ torr). This new pressure is called the oxygen partial pressure. The temperature of the substrate and the oxygen partial pressure during growth are two of the main parameters to control during an MBE growth.

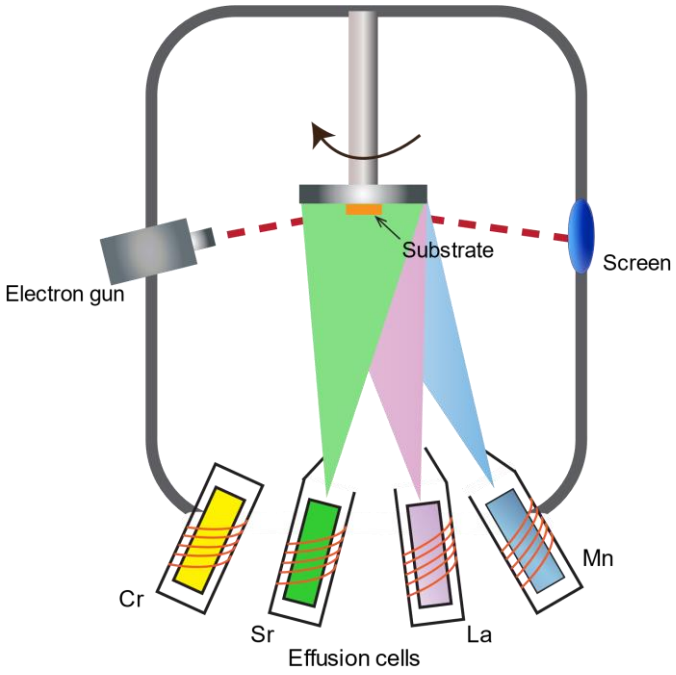

Figure 2.1. Illustration of a basic MBE set up. The bottom of the chamber is equipped with effusion cells which heat the elements to their sublimation temperatures. The molecular beam is deposited on a substrate which is heated to provide energy for the crystal to form. An electron gun is used to diffract electron from the substate during growth and is captured by a phosphorous screen. (S. Koofar) [1]

2.1.2 Reflection high energy electron diffraction (RHEED)

A powerful tool that is used before, during and after growth is reflection high energy electron diffraction. Electrons with 15 keV of kinetic energy are accelerated towards the substate at shallow angles. The electron beam diffracts, and a pattern is collected on a phosphorus screen. This diffraction pattern can give us information about the crystal structure of the substrate such as its degree crystallinity (single crystalline, polycrystalline or amorphous), the roughness of the surface, as well as its basic symmetry. Monitoring the diffraction pattern during growth can give

valuable information about the growth process. During the growth of the film, the intensity of the diffraction pattern will oscillate as each monolayer of the film is completed. By counting the number of oscillations, the number of monolayer and subsequently, the thickness of the film can be monitored and controlled. The result is that we can achieve atomic layer precision in the desired thickness of our films

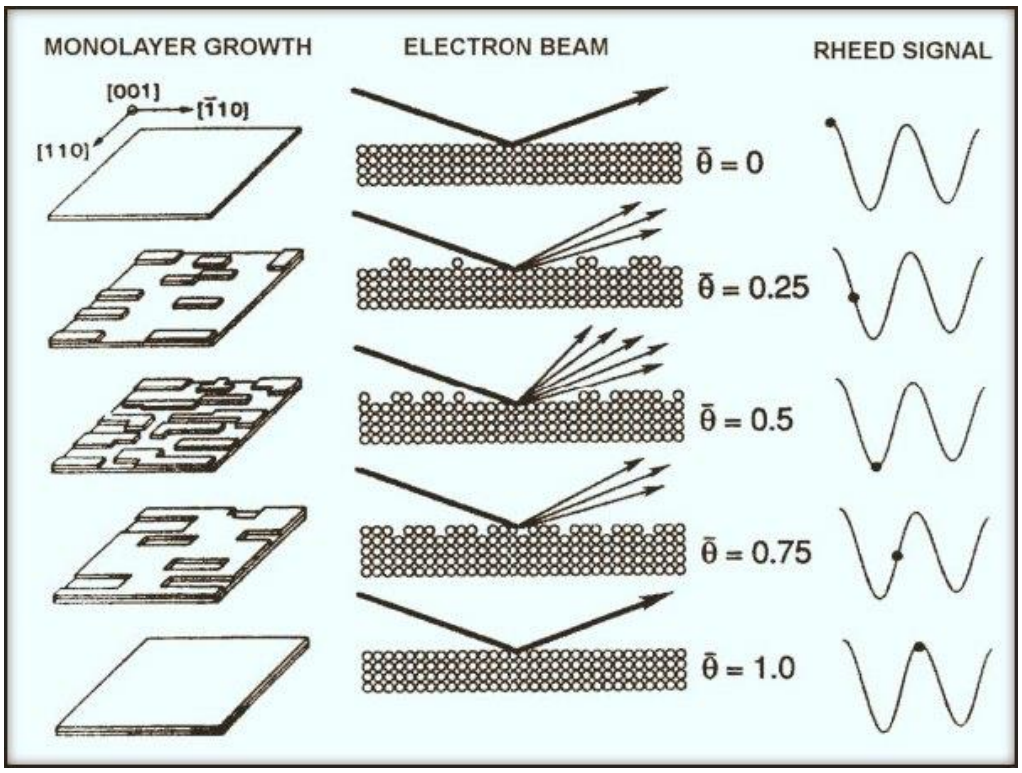

Figure 2.2. Image explaining the mechanism behind RHEED. In an island growth mode where small islands of a unit cell of a crystal form, the surface roughness of the crystal varies as the monolayer is forming. Halfway through the grow of a unit cell when the surface roughness of the film is at a maximum, the diffraction intensity is at a minimum. As the layer completes and a full layer is deposited, the surface becomes smooth again and the diffraction intensity returns to before. The number of oscillations in the diffraction intensity correspond to the number of unit cells deposited. (Neave) [2]

2.2 Transport properties

2.2.1 Sheet resistance, sheet carrier concentration and mobility

The electrical resistance of a material is a measure of how easily electrical current can travel through a material. The resistance of a material depends on both the material property and its geometry. To obtain a material dependent characteristic only, we must measure the resistivity or sheet resistance of a material. We have chosen to measure the sheet resistance of our samples as it is easier and does not require making assumptions about the thickness of our conducting layer. We use the Van der Pauw method to measure the sheet of our sample. Figure 2.3 shows a diagram of how the sample is prepared. Gold contacts are deposited on the corners of our sample and aluminum wires are bonded from the corners of the sample to a small copper plate which is connected to an ammeter and a voltmeter. The gold contacts are to insure good ohmic contact between our sample and measurement system. Current is sourced in one direction while the voltage is measured on the opposite side. The procedure is repeated for the other direction. Dividing the measured voltage by the source current gives the two components of the sheet resistance, R_A and R_B. If R_A and R_B are close in value, then the sheet resistance R_s can be calculated by:

$$R_s = \frac{\pi * avg(R_A, R_B)}{\ln(2)} \tag{2.1}$$

Where avg(R_A,R_B) denotes the average of R_A and R_B.

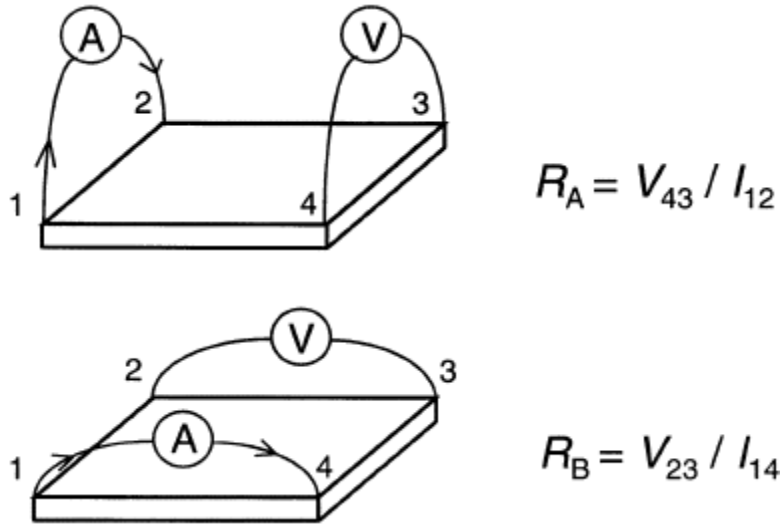

Figure 2.3. Example of a Van Der Puaw electrical set up. For a square sample, the current I_{12} & I_{14} are sourced from one side and the voltage V_{43} & V_{23} are measured on the opposite side. The resistance is obtained by dividing the measured voltage by the sourced current. The process is repeated for the completing side. (Rietveld) [3]

2.2.2 Magnetoresistance

The resistance of a material can be measured as a function of applied magnetic field. Typically, the data is normalized to the resistance at zero field and is expressed as a percent versus applied field. As such, the actual value of the resistance doesn't matter and a 2pt resistance measured diagonally is used when performing MR measurements for our sample. Figure 8 is an illustration of the set up for a MR measurement. The relationship between the applied magnetic field strength and direction verses the measured resistance of the sample can give information about the scattering mechanisms and confinement of the carriers.

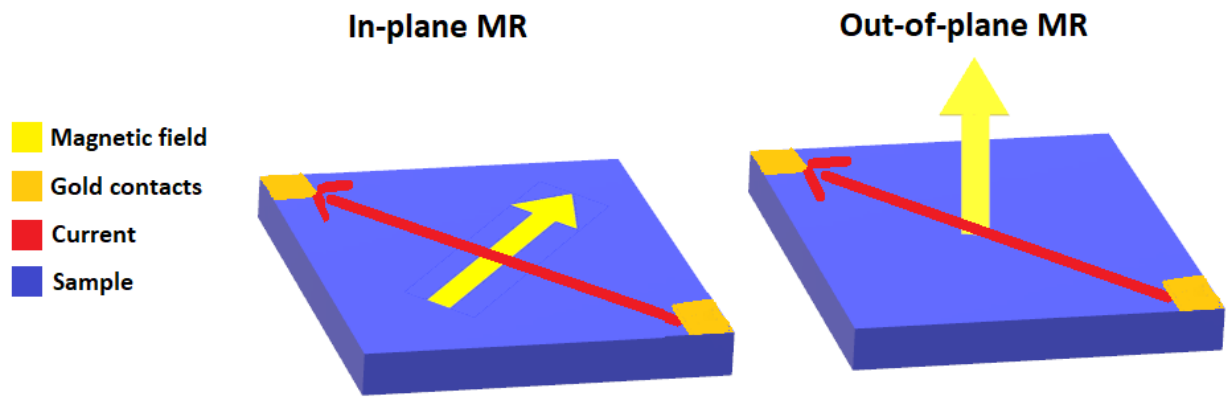

Figure 2.4. Illustration of the experimental set up of a magnetoresistance measurement. On the left the magnetic field is in plane to the sample but perpendicular to the current. On the right the magnetic field is out of plane of the sample.

2.2.3 Physical properties measurement system (PPMS)

The physical property measurement system (ppms) by quantum design Inc. is a versatile multi-purpose laboratory equipment. Sample mounts have 12 electrical leads which insert into the bottom of the cryostat. Sample are glued to the mount using GE varnish. Two sample can fit on the sample mount at a time which allows for a more time efficient use of the system. Once loaded into the cryostat, the ppms can make electrical measurements from 400K-2K and from ± 7 Tesla.

Figure 2.5 (On the left) Picture of a sample puck where our samples are mounted. (On the right) physical property measurement system by quantum design. (Quantum Design Inc) [4]

2.3 Electronic structure characterization

2.3.1 X-Ray photo-emission spectroscopy (XPS)

XPS is a widely used experimental technique used to probe the electronic state of a material. X-rays of a specific energy are focused onto a sample. The X-rays eject electrons from the material via the photoelectric effect and are collected by a detector which measures the number of electrons ejected and their kinetic energy. The difference between the kinetic energy of the electron and the energy of the incident X-ray gives the bind energy of that electron. Because X-rays are high energy photons, they can eject electrons with large binding energies. This allows for the measuring both the core levels of the elements, as well as the electrons which occupy the valence bands.

XPS is a valuable technique when studying the electronic structure of thin films. By measuring the onset of energy absorption, the valence band edge (VBE) can be measured.

However, this requires the presence of a single material in the measured spectra as not to confound which VBE is being measured. By comparing the VBE of bulk material and the substate as well as comparing any shifts in the binding energy of core levels in a thin film (where the spectra is from both substrate and film is collected), the band alignment can be determined.

2.3.1 Laser angle resolved photo-emission spectroscopy (L-ARPES)

Laser angle resolved photo-emission spectroscopy is an advanced experimental technique which share many commonalities with XPS. There are two main differences between them. First, is that a laser light source is used instead of X-rays to excite the electrons. The use of a laser with wavelengths from the infrared to the ultra-violet limits us to measuring the electronic state near the fermi energy. However, since a laser's light source is much more monochromatic, a higher energy resolution can be achieved than in a typical laboratory XPS instrument. This allows us to resolve the band structure of a materials much more accurately than in XPS. In addition, the escape depth of electrons is much shallower than XPS which means that L-ARPES is much more sensitive to the surface of a thin film. The second difference is that momentum of the ejected electron is measured along with its kinetic energy. The resolution of the momentum allows for the mapping of a band structure (E vs k) and give addition information about the material.

2.3 Structural Characterization

2.3.1 X-ray diffraction

X-ray diffraction a powerful experimental technique which is commonly used in the material science field to characterize the structure of materials. For single crystals, a monochromatic and collimated beam of X-rays are directed to the crystal. The X-rays scatter off

the crystal into a diffraction pattern which are collected by a detector. The diffraction pattern takes the form of peaks which occur at specific angles of incident and refection. Where these peaks are located depend highly on the structure of the crystal. The intensity of the diffraction pattern *I* is proportional to the structure factor *F* of the film.

$$I \propto \| F \|^2 \tag{2.2}$$

The structure factor is defined as follows:

$$F = \sum_n f_n \, e^{-\frac{w}{2}} e^{2\pi i(hx_n + ky_n + lz_n)} \tag{2.3}$$

Where f_n is the atomic form factor, w is the Debye Waller factor, hkl are the miller indices of the crystal and x_n y_n z_n are the positions of the atoms in the unit cell. The structure factor is summed over all the atoms in the unit cells.

To acquire the structure of a thin film, the intensity of the diffracted beam is measured along specific crystallographic directions h, h, l. of the substate. This is achieved by rotating the detector, sample or source. For a bulk crystal there should only be peaks at integer values of h,k,l. However due the 2D nature of thin films, the intensity is non-zero between Bragg peaks. These measurement of intensity between the Bragg peaks of the crystal substate are called Crystal truncation rods (CTRs)[5].

Due to the small volume of our thin films (~4nm thick) the measured intensity in typical laboratory X-ray diffractometers would be too weak to measure. To collect high quality data, we use synchrotron source for our X-ray experiments. Synchrotron X-ray sources unlike typical laboratory sources produce X-rays by undulating or wiggling an electron beam moving near the speed of light. The intensity of the beam is orders of magnitude brighter than a typical laboratory

source. However, this requires a particle accelerator which are too large (~ mile in diameter) and cost prohibitive to be found in a typical university laboratory. To collect our data, we performed our XRD experiments at the Advanced Photon source at Argonne national lab in Illinois.

The detector used is a 2D Pilatus detector which captures the diffracted beam and maps the counts per second per pixel. The intensity of the peak is extracted by subtracting the peak intensity from the background. Each image we extract corresponds to an intensity of the peak at a specific crystallographic location. This process is done for each measured rod until we have a satisfactory number of rods.

Once we have a set of rods, we load the data into a the GenX software [6]. GenX is a free XRD analysis software we use to determine the structure of our films. We start by giving it a starting model of the film. The software uses the model to calculate the structure factor of the film and convert it into an intensity vs reciprocal lattice parameter. It then compares the simulated intensity vs the measured intensity and calculates the error between them. There are many different error functions, but we use the crystallographic R1 and the LogR1 error function. Those functions are defined as follows:

$$FOM_{R1} = \sum_i \frac{\sqrt{(Y_i)} - \sqrt{(S_i)}}{\sqrt{(Y_i)}} \tag{2.4}$$

$$FOM_{LogR1} = \sum_i \frac{log_{10}(\sqrt{(Y_i)}) - log_{10}(\sqrt{(S_i)})}{log_{10}(\sqrt{(Y_i)})} \tag{2.5}$$

Where Y_i is the experimental value of the intensity and S_i is the simulated intensity. GenX then modifies parameters of our choice, typically the lattice parameter of each unit cell, Debye Waller factors and even the occupation of certain elements. After it modifies the parameters, it recalculates the structure factor and compares the intensity of the new model to the experimental

data. If the new model has less error between it and the experimental result, then it keeps the new model, otherwise it discards it and tries again. The process is performed iteratively until the error between the model and the experimental data is minimized.

REFERENCES

[1] S. Koofar, *Phd Thesis*, **2019**, page 77.

[2] Neave, J. H., et al. *Applied Physics A*, **1983**, 31.1 1-8.

[3] Rietveld, Gert, et al., *IEEE transactions on instrumentation and measurement*, **2003**, 52.2, 449-453.

[4] Quantum Design of North America, *https://qdusa.com/products/ppms.html*, picture, **2020.**

[5] I. Robinson and D. Tweet, *Rep. Prog. Phys*. 55, 599 **1992**.

[6] M. Björck and G. Andersson, *J. Appl. Crystallogr*. **2007**. 40, 1174.

CHAPTER 3

Growth-Temperature Dependence of Conductivity at the LaCrO3/SrTiO3 (001) Interface

This chapter is based upon the following publication:

A. Al-Tawhid, J. Frick, D. B. Dougherty, D. P. Kumah, *JVST A*, 37 (2), p. 021102. (2019).

Contributions:

The author grew the materials and performed the X-ray diffraction and structure analysis and the electrical transport measurement.

3.1 Preface

The effect of growth conditions and postgrowth treatment on the structural and electronic properties of the polar/nonpolar $LaCrO_3/SrTiO_3$ (LCO/STO) interface has been investigated. Under low oxygen partial pressure, oxygen vacancies are formed in the STO substrate resulting in metallicity with a measured sheet carrier concentration of 10^{16} cm $^{-2}$. Annealing postgrowth in flowing oxygen causes the sheet carrier concentration to saturate to 10^{13} cm $^{-2}$, which is consistent with the reported values of a two-dimensional gas at other polar/STO interfaces. However, growth under nonreducing growth conditions leads to insulating behavior. High-resolution synchrotron x-ray-based structural determination of the atomic-scale structures of both metallic and insulating LCO/STO interfaces shows chemical intermixing and an interfacial lattice expansion.

3.2 Introduction

Polar/nonpolar perovskite interfaces have attracted considerable interest since the discovery of novel interfacial phenomena not found in the constituent bulk materials.[1–4] Of considerable interest is the interface between polar LaAlO3 (LAO) and nonpolar SrTiO3 (STO), which exhibits a high mobility quasi-two-dimensional electron gas (q-2-deg), ferromagnetism, and superconductivity, despite both materials being nonmagnetic bulk insulators.[1,2,5] Conductivity at the LAO/STO interface has been attributed to an interfacial polarity driven electronic reconstruction,1 ionic intermixing[6] and defects related to cation nonstoichiometry,[7] and oxygen vacancies.[8] Since its discovery, other complex oxides such as $SmTiO_3$, $GdTiO_3$, $LaTiO_3$, $LaGaO_3$, $LaVO_3$, and $NdTiO_3$ have been grown on STO and have been shown to also exhibit interfacial conductivity,[9–16] while some polar/nonpolar interfaces such as the $LaCrO_3$ (LCO)/STO) were found to be insulating.[17]

An electric field at the LCO/STO interface observed by photoelectron spectroscopy[17] is expected to result in an electronic reconstruction resulting in a conducting interface. The absence of conductivity is attributed to Ti out diffusion, which results in a redistribution of charge in the interfacial CrO_2 layers.[17] However, mobile charge carriers have been reported for LCO/ STO superlattices.[18] To gain further insight into the intrinsic and extrinsic mechanisms that trigger conduction at these interfaces, the effect of growth conditions is required. In this paper, we investigate the effect of growth temperature and postgrowth treatment on the electrical and structural properties of the LCO/STO interface using a combination of high-resolution synchrotron x-ray diffraction structural measurements, angle-resolved photoemission spectroscopy (ARPES), and temperature-dependent transport measurements.

Previous reports on the LAO/STO interface have shown that growth temperature can have a considerable effect on the transport properties of the interface.[19] Here, we find that by varying the growth temperature and postgrowth treatments, the interface can be tuned from an insulating to a high mobility metallic state. Samples grown at a lower temperature (600 ^{o}C) are insulating while higher growth temperatures (800 ^{o}C) under identical oxygen pressures lead to metallicity. The as-grown sample exhibits sheet carrier concentration on the order of 10^{16} cm $^{-2}$ which is similar to that of LAO/STO interfaces under similar growth conditions as well as oxygen reduced STO.[20] Annealing the metallic samples in flowing oxygen causes the reduction in the sheet carrier concentrations to 10^{13} cm $^{-2}$, as well as a change in color from gray to clear, which we attribute to the reduction of oxygen vacancy concentration in the bulk STO. There is an expansion of the out-of-plane lattice constant of the STO at the interface in both samples which we attribute to the La–Sr interdiffusion. The necessity of a reducing environment for the interfacial conductivity to occur points to defects related to oxygen vacancies as the origin of the interfacial metallicity.[18]

3.3 Experimental methods

3.3.1 Growth and treatment

LCO films with a nominal thickness of 10-unit cells (uc) were grown on (001) oriented STO substrates by molecular beam epitaxy (MBE). Prior to growth, the STO substrates were treated with buffered HF and annealed in flowing oxygen at 1000 ^{o}C in a tube furnace for 2 h to create a Ti terminated surface.[21] Atomic force microscope (AFM) images of the substrate after treatment show that the terrace step structure is present. The LCO films were grown at 1x10^{-7} Torr oxygen partial pressure with the base pressure of the MBE chamber being 2 x10^{-10} Torr. The flux of the La and Cr sources was calibrated before growth with a quartz crystal microbalance. In situ

reflection high energy electron diffraction (RHEED) was used to monitor the growth process. Images of the RHEED pattern of a bare STO and a 10 uc LCO are shown in Figs. 3.1(a) and 1(b), respectively. RHEED oscillations of a 10 uc LCO in Fig. 1(c) indicate that layer-by-layer growth is achieved, and the number of layers deposited is determined by the number of RHEED oscillations. AFM images after growth of the LCO [Fig. 1(d)] show that the terrace step structure of the STO substrate is preserved confirming epitaxial growth.

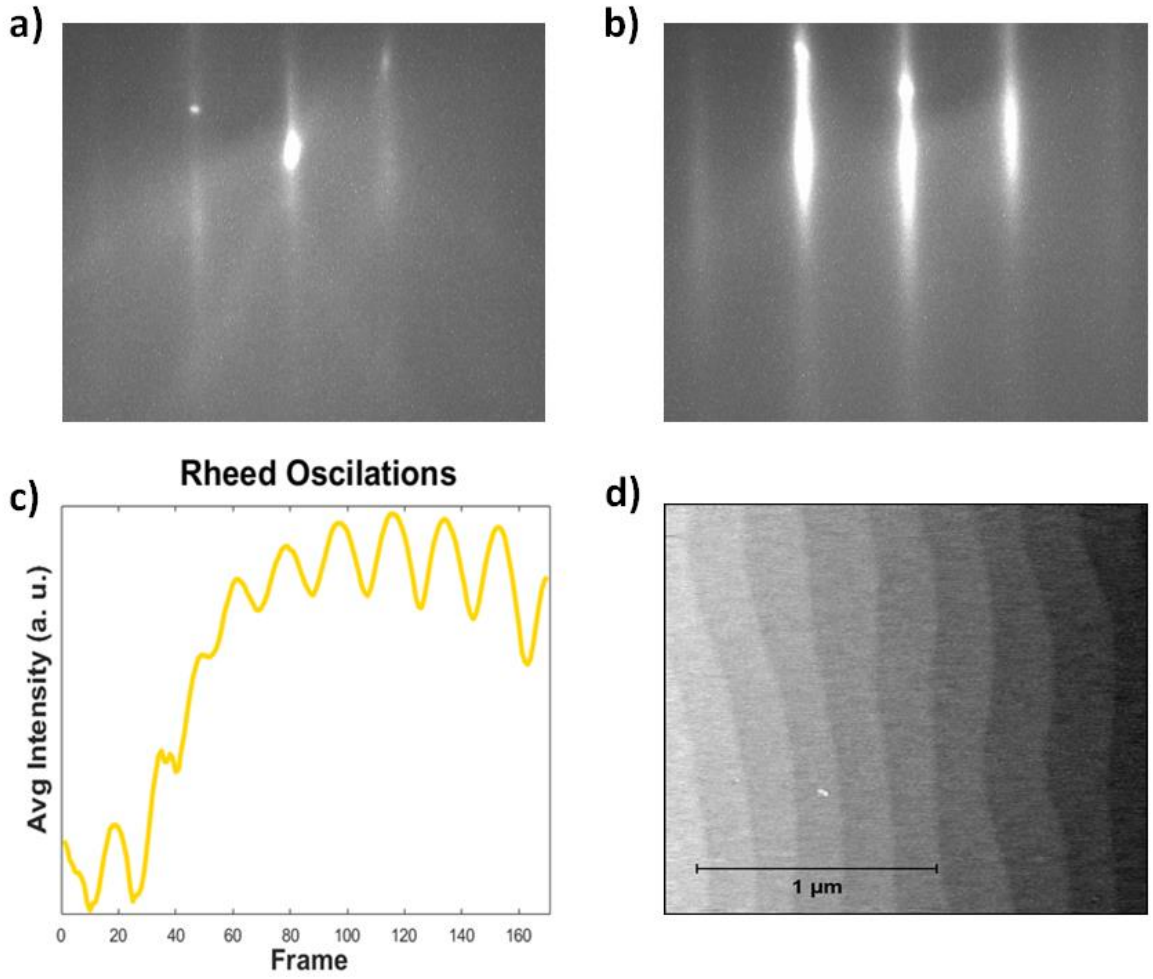

Figure 3.1 Growth properties of LCO films grown on STO by molecular beam epitaxy. (a) RHEED image of the bare STO substrate. (b) RHEED image of 10 uc LCO on STO after growth and (c) RHEED oscillations for a 10 uc LCO film grown at 800°C and 1×10^{-7} Torr O_2. (d) AFM image of a 10 uc LCO. Note that the terrace step structure is preserved with a step height of 4 Å.

The samples were grown in two temperature regimes; a high temperature regime (800 ^{o}C) (henceforth referred to as HT) and a low temperature regime (600 ^{o}C) (henceforth referred to as LT). The HT samples were then split into two groups; a set of samples that were annealed ex situ in a tube furnace at 400 ^{o}C with flowing pure (99%) oxygen for 4 h and a second set that was left untreated.

3.3.2 Transport/Hall measurements

Temperature-dependent Hall and resistivity measurements were performed using a 4-point Van der Pauw configuration in the range of 2–300 K. Gold contacts were deposited at the corners of the samples using a shadow mask. All transport measurements were performed using a Quantum Design physical property measurement system. Both as grown and annealed samples were found to be metallic at room temperature with sheet resistivities on the order of 100 and 30 kΩ/□, respectively. The LT samples were too insulating to measure their sheet resistance which we estimate to be greater than 100 MΩ/□.

3.3.3 Synchrotron X-ray diffraction

To determine the differences in the atomic-scale structures of the as-grown HT-metallic and LT-insulating nominally 10 uc LCO films, synchrotron x-ray diffraction measurements were carried out at the 33ID beamline at the Advanced Photon Source. Crystal truncation rods (CTRs)[22] were measured along the STO bulk crystallographic directions with an incident x-ray energy of 15.5 eV. The layer-resolved structure and the composition of the films were obtained from fitting the CTR data with a genetic-based algorithm, GenX.[23]

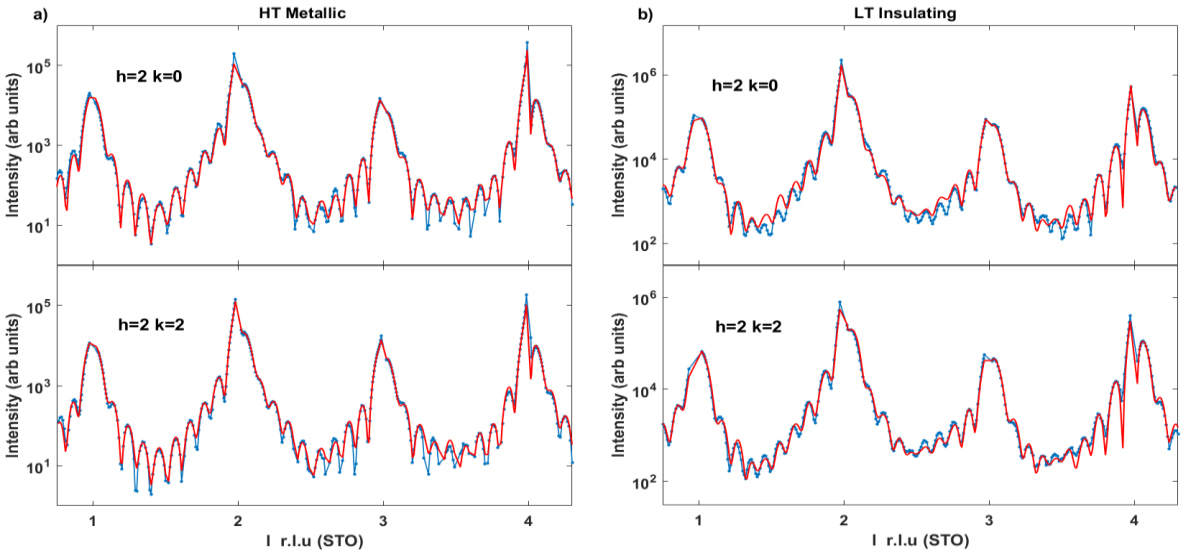

Figure 3.2. Representative measured and calculated CTRs for (a) an HT as-grown 10 uc LCO/STO heterostructure grown at 800◦C and (b) an LT as-grown 10 uc LCO/STO heterostructure grown at 600◦C. The h, k, and l values are in units of the bulk cubic $SrTiO_3$ reciprocal lattice vectors.

The parameters of the fit included the out-of-plane lattice constant of each layer, Debye-Waller factors for each element, and the fractional occupation of the surface LCO layer to account for surface roughness. Additionally, the chemical composition of the first five layers of the film and the substrate at the film/substrate interface were optimized to allow for intermixing. Each element was also allowed to displace in the (001) direction, and the oxygen octahedral was allowed to rotate and tilt. [24,25] The fit was then compared to the data iteratively to minimize the error between them. Structural convergence was achieved by minimizing the crystallographic R1 error function. We obtain excellent fits with figures of merit values below 0.08 for each fit. Representative measured CTRs and their associated fits for the HT and LT as-grown samples are shown in Figs. 3.2(a) and 2(b), respectively.

3.3.4 Angle Resolved photoemission spectroscopy

To determine if the changes to conductivity were related to changes in the electronic structure of the LCO films, FIG. 1. Growth properties of LCO films grown on STO by molecular beam epitaxy. (a) RHEED image of the bare STO substrate. (b) RHEED image 10 uc LCO on STO after growth and (c) RHEED oscillations for a 10 uc LCO film grown at 800 ^{o}C and 1x10^{-7} Torr O_2. (d) AFM image of a 10 uc LCO. Note that the terrace step structure is preserved with a step height of 4 Å. ARPES was performed at room temperature (27 ^{o}C) in ultrahigh vacuum using both an He I (21.2 eV) plasma light source and a pulsed laser source (6.2 eV from the fourth harmonic of a Ti-sapphire laser). Photoelectrons were analyzed using a 150 mm mean radius hemispherical analyzer (Specs Phoibos 150) with a 2D detector. All samples were transported from the growth chamber through ambient air to be inserted in the ARPES chamber. They were subsequently annealed in vacuum at 300 ^{o}C for 30 min and allowed to cool back to room temperature prior to data collection. The binding energy scale on all samples was corrected for charging effects in order to correspond with Maiti and Sarma.[26]

3.4 Results and discussion

To determine the effect of the growth conditions on the structural properties of the LCO/STO interface, the layer resolved atomic-scale structures were determined from fits to CTRs measured by synchrotron x-ray diffraction. The structural properties of as-grown HT and LT samples are compared in Fig. 3.3. Figure 3.3(a) shows the A-site composition along the growth direction for the LT and HT samples. The chemical profile across the interface shows that significant La/Sr interdiffusion occurs for both insulating and metallic samples in agreement with previous electron microscopy and Rutherford backscattering measurements which has been

suggested to be driven by strain relaxation.[27] For both the HT and LT samples, a tail of Sr out diffusion into the LCO film extends about 4–5 layers away from the interface [layers 1–5 of Fig. 3.3(a)] decaying from 25% in the first interfacial LCO layer.

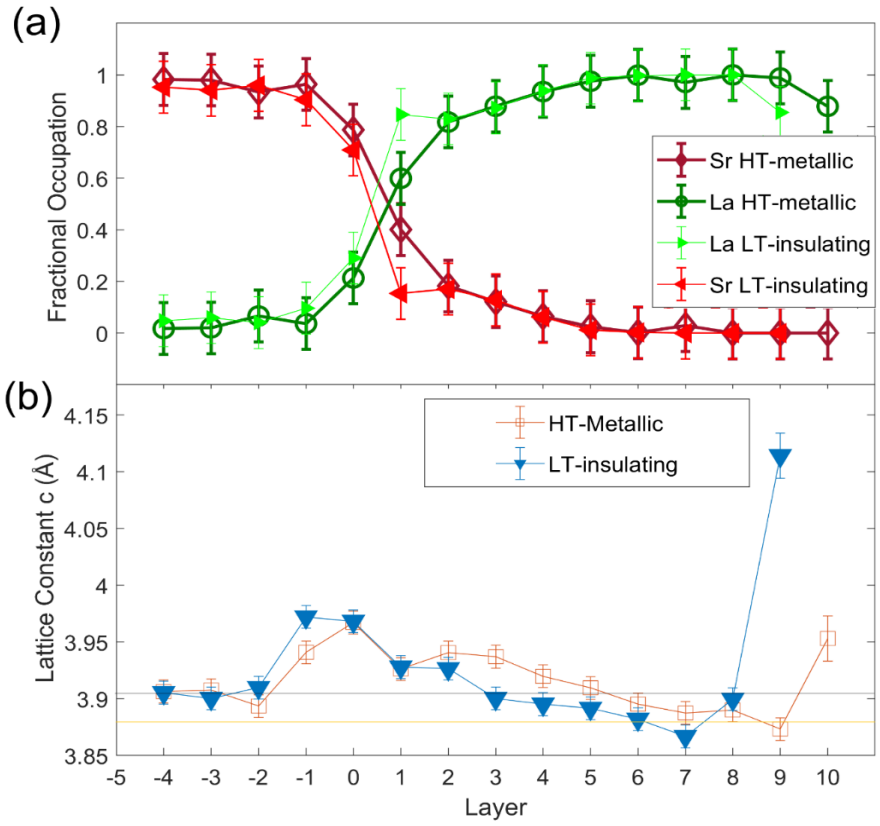

Figure 3.3. (a) Layer-resolved Sr/La occupation for metallic as 800°C and insulating 600°C as-grown LCO samples. (b) Layer-resolved out-of-plane lattice constant for metallic as 800°C and insulating 600°C as-grown LCO samples. Layer 0 indicates the top of the STO substrate. The expected out-of-plane lattice constants of STO (3.905 Å) and LCO (3.88 Å) are indicated by horizontal lines on the plot.

Due to the comparable atomic scattering factors of Cr (24 electrons) and Ti (22 electrons) at 15.5 keV and the ability of the B cations to occupy different oxidation states, the uncertainty associated with the B-site composition profile is too large to draw relevant conclusions. However,

high-resolution electron microscopy measurements show Cr–Ti interdiffusion occurring at the LCO/STO interface. [27,28]

The layer-resolved lattice constants shown in Fig. 3.3(b) are determined from the spacing of the A-site cations along the growth direction. We observe in both samples an expansion at the interface followed by a linear decrease toward the film surface. The expansion in the STO (layers 1 and 0) which is also observed in LAO/STO interfaces is related to the diffusion of La into the STO substrate.[6,24] La substituting for Sr would donate an electron and alter the valence state of Ti from +4 to +3 increasing its ionic radius. For stochiometric LCO films coherently strained to STO, the expected out-of-plane lattice constant is 3.88 Å for an LCO Poisson ratio of 0.23.28 The larger lattice constant in both the HT-metallic and the LT-insulating LCO film may be related to La–Sr and Cr–Ti interdiffusion and/or oxygen vacancies in the LCO. The HT as-grown samples show a larger average lattice constant which is likely due to the higher concentration of oxygen vacancies.[29,30] In both samples, we observe a large lattice expansion at the film surface which is likely due to structural distortions and the polar discontinuity at the film vacuum interface.[24]

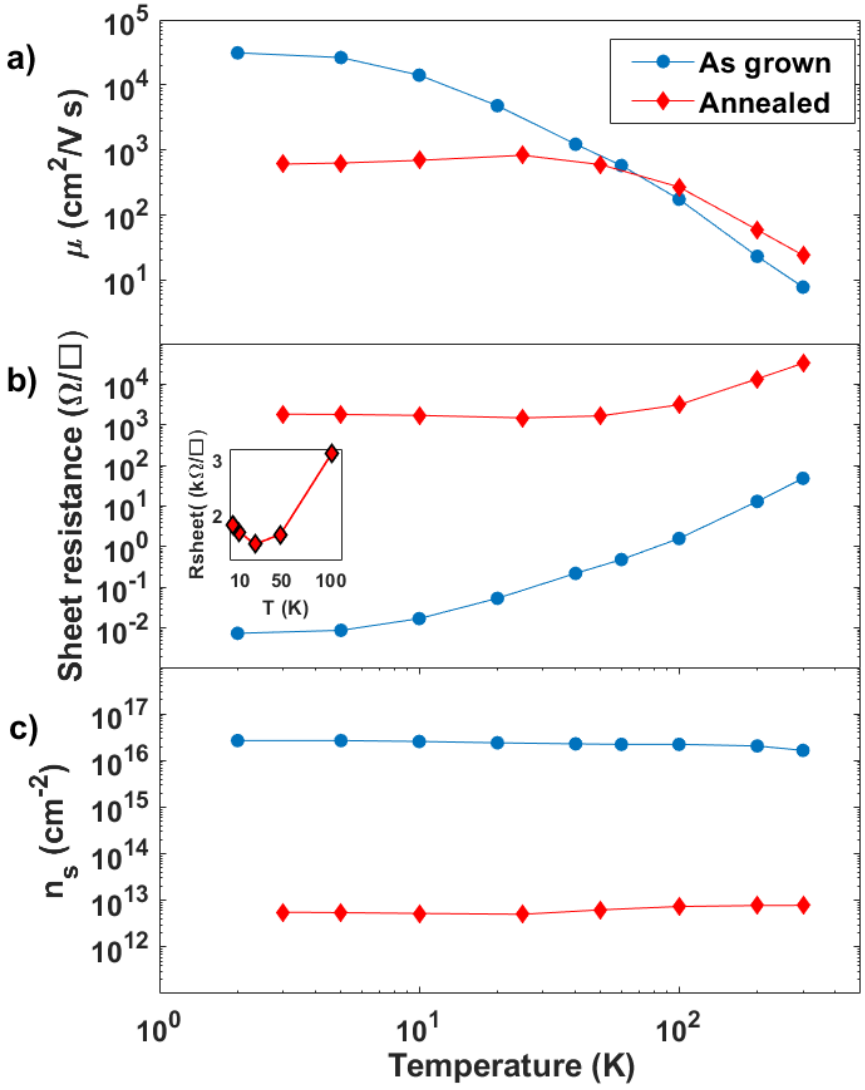

Figure 3.4. (a) Comparison of mobility, μ, (b) sheet resistance, and (c) sheet carrier density, ns, as a function of temperature for a 10 uc LCO/STO grown at 800 °C without a postgrowth anneal and a 10 uc LCO/STO grown at 800°C followed by an anneal in 1 atm 99.99% O_2 at 400°C for 4 h. The inset shows sheet resistance of the annealed sample at low temperature to highlight the upturn.

Figure 3.4 shows the temperature-dependent mobility (μ), sheet resistance, and sheet carrier density (ns) for the LCO/ STO samples determined from the Hall measurements. The transport properties are compared for the HT as grown and postgrowth annealed samples. The as-

grown sample shows a sheet carrier density of 10^{16} cm^{-2}, which indicates that the majority of the carrier are found in the reduced STO substrate.[20] This is corroborated by the fact that the temperature dependence of the sheet resistance and mobility is similar to previous reports of reduced STO and LAO/STO interfaces grown under low oxygen growth pressures without postgrowth annealing.[1,20] Upon annealing, the oxygen vacancies are reduced, and the sheet carrier concentration saturates to approximately 10^{13} cm^{-2}. The temperature dependence of the sheet resistance reduces, and a minimum occurs at 30 K followed by an upturn. The upturn at low temperatures is possibly due to weak localization or Kondo scattering. The source of Kondo scattering may be either magnetic Ti3+ or Cr.[16,31–33] These results are similar to LAO/STO heterostructures which have been grown under the reducing condition and then annealed post growth in an oxygen-rich environment or grown at high oxygen partial pressure.[20,31]

In contrast, the LT samples were found to be completely insulating with RT sheet resistances greater than 100 MΩ/□. This result is similar to previous reports of LCO/STO heterostructure grown at 650 ºC and 6 $x10^{-8}$ Torr partial oxygen pressure.[17,28] Annealing LT samples in the growth conditions of HT samples (107 Torr partial O2 pressure and 800 ºC) causes a high concentration of oxygen vacancies to form in the STO substrate as evidenced by its high sheet carrier concentration (10^{16} cm^{-2}) as well as a gray discoloration of the sample. However, upon annealing the sample in flowing oxygen at 400 ºC, the sample returns to its previous insulating state. This result suggests that reducing conditions are necessary during the growth for interfacial conductivity to occur.

The necessity of the reducing condition (high temperature and low oxygen partial pressure) during growth suggests that oxygen vacancies in either the STO or the LCO play an important role in the formation of the 2-deg. Doping due to cation intermixing can be ruled out as the main source

of conductivity as it is observed in both the insulating and metallic samples in Fig. 3.4. Hole doping of LCO with Sr can induce an insulator-metal transition for Sr dopants above 65%.[34] However, the Sr content observed for both films in Fig. 3.3(a) is insufficient to account for the metallicity. Additionally, the Hall coefficient for the metallic samples is negative indicative of majority electron carriers.

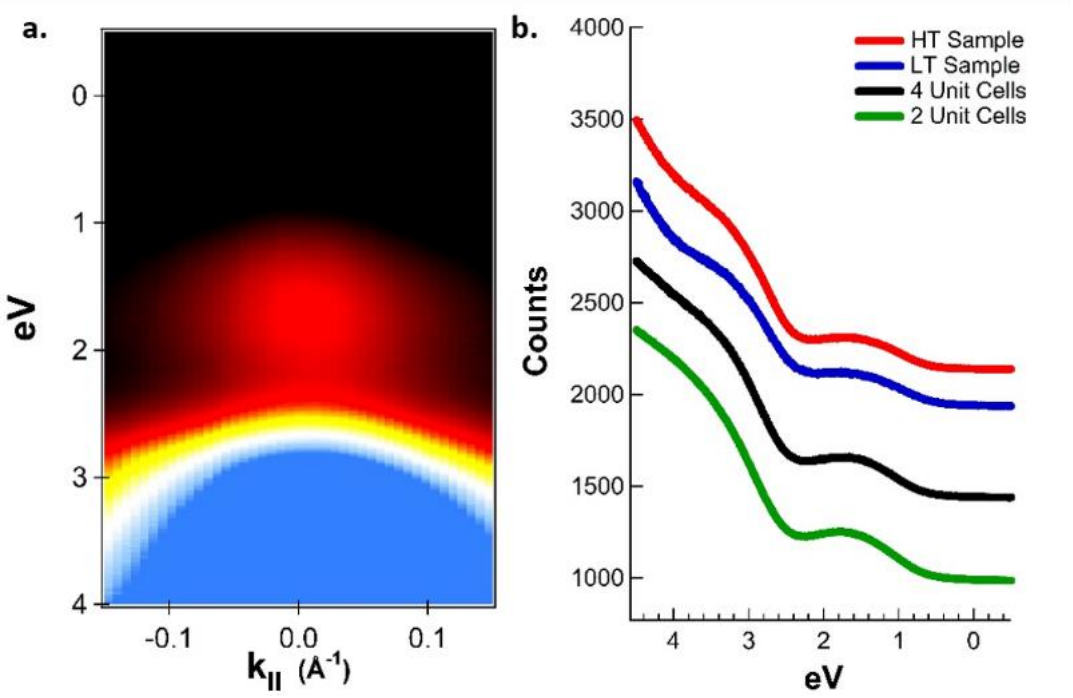

Figure 3.5. (a) Angle-resolved photoemission spectra of 4 unit cell HT LaCrO3 thin film; (b) line cuts at k=0 of a thick (bulk-like) HT LaCrO3 sample, thick LT sample, 4 unit cell thick HT sample, and 2 unit cell HT sample. The line cuts are stacked vertically for clarity.

Angle-resolved photoelectron spectroscopy measurements were carried out to elucidate the electronic structure near the surface of the LaCrO3 films. Figure 5(a) shows ARPES measurements of a 4-unit cell LaCrO3 film grown under high temperature conditions that was verified by

resistivity measurements to show metallic behavior. Between 1 eV and 2 eV, we find a state assigned predominantly to the Cr 3d valence orbitals, while the more deeply bound state (2.5– 4.0 eV) comes predominantly from O 2p orbitals.[26] The data shown in Figs. 3.5(a) and 3.5(b) are representative of all films studied under different thicknesses, different photon energies, and different substrate temperatures during growth. Despite these numerous different conditions, all ARPES measurements showed precisely the features seen in Fig. 5(a). No photoelectron intensity near the Fermi level (0.0 eV) is observed for any of the LCO films considered [Fig. 5(b)]. Some minor differences in the valence band spectra may exist due to the differences in the secondary electron background and in the defect density between the films. Nevertheless, the photoemission observations show that the electron structure near the surfaces of each film is essentially identical. The results shown in Fig. 3.5 correspond to 21.2 eV photon energies, which result in photoelectrons with very short escape depths, and thus sensitive mostly to the surface of the film. By extending our measurements down to 2-unit cell films [lowest spectrum in Fig. 3.5(b)], we confirm that the metallic transport behavior is not occurring in the LCO film.

A possible mechanism responsible for the formation of the 2-deg at the HT LCO/STO interface involves the formation of oxygen vacancies at the LCO/STO interface, the bulk STO substrate, and the LCO film as evidenced by the high sheet carrier concentration (10^{16} cm^{-2}) and the expansion of the LCO lattice. Here, oxygen vacancies form during growth due to a redox reaction between the oxygen-deficient LCO film and the STO substrate and are stabilized at the interface.[35,36] Upon annealing in oxygen, oxygen vacancies in the bulk STO and film are removed, while at the interface, the vacancies are trapped. For amorphous LAO films grown on the STO under reducing growth conditions, a redox reaction between the film and the TiO2-terminated STO

surface has been proposed to result in oxygen vacancies in the STO layers close to the interface which contributes to metallicity.[37]

To verify the necessity for the reducing conditions for interfacial metallicity, we grew an insulating sample under oxidizing conditions. For growth under low temperature, the redox reaction is suppressed resulting in an insulating interface. [28,36] This sample was annealed in vacuum resulting in metallicity with a sheet carrier concentration of 10^{16} cm^{-2} indicative of bulk metallicity. A post anneal in oxygen at 400 ^{o}C resulted in insulating transport behavior. We note that additional mechanisms including charge transfer induced by the oxygen vacancies may contribute to the interfacial conductivity and further studies are required to elucidate their role.[20]

3.5 Conclusion

In summary, we have shown that growth conditions play a critical role in the creation of mobile charge carriers in LCO/STO(001) heterostructures. Under nonreducing conditions, both the substrate and the film are completely insulating. Under reducing conditions (high growth temperature, low oxygen pressure), oxygen vacancies form in the bulk STO as evidenced by high sheet carrier concentrations. However, postgrowth annealing in pure oxygen at 400 ^{o}C causes a reduction in the oxygen vacancies and a sheet carrier concentration that saturates to approximately 10^{13} cm^{-2}. The electrical properties of the LCO/STO interface show remarkable similarities to the 2-deg at the LAO/ STO interface, suggesting that they share a common origin. Structurally, both insulating and metallic LCO/STO samples exhibit significant La/Sr intermixing and an expansion of the out-of-plane lattice constant at the interface. The HT samples show a larger average lattice constant in the film suggesting a higher concentration of point defects, most likely in the form of oxygen vacancies. Further work is required to investigate the effect of the proximity of

antiferromagnetic LCO [40–42] on the magnetoresistance and superconductivity [5] observed at polar oxide/STO interfaces.

REFERENCES

[1] A. Ohtomo and H. Hwang, *Nature* 427, 423 **(2004)**.

[2] A. Brinkman et al., Nat. Mat. 6, 493 (**2007).**

[3] F. J. Wong, S.-H. Baek, R. V. Chopdekar, V. V. Mehta, H.-W. Jang, C.-B. Eom, and Y. Suzuki, *Phys. Rev. B* 81, 161101 (2010).

[4] J. Mannhart and D. Schlom, *Science* 327, 1607 **(2010).**

[5] N. Reyren et al., *Science* 317, 1196 **(2007).**

[6] P. Willmott et al., *Phys. Rev. Lett*. 99, 155502 **(2007).**

[7] E. Breckenfeld, N. Bronn, J. Karthik, A. Damodaran, S. Lee, N. Mason, and L. Martin, *Phys. Rev. Lett.* 110, 196804 **(2013).**

[8] G. Herranz et al., *Phys. Rev. Lett*. 98, 216803 **(2007).**

[9] P. Perna et al., *Appl. Phys. Lett.* 97, 152111 **(2010).**

[10] P. Moetakef, *Appl. Phys. Lett.* 99, 232116 **(2011).**

[11] L. Kornblum, E. N. Jin, D. P. Kumah, A. T. Ernst, C. C. Broadbridge, C. H. Ahn, and F. J. Walker, *Appl. Phys. Lett.* 106, 201602 **(2015).**

[12] P. B. Marshall, E. Mikheev, S. Raghavan, and S. Stemmer, *Phys. Rev. Lett.* 117, 046402 **(2016).**

[13] C. He, T. Sanders, M. Gray, F. Wong, V. Mehta, and Y. Suzuki, *Phys. Rev. B* 86, 081401 **(2012).**

[14] K. Ahmadi-Majlan et al., *Appl. Phys. Lett*. 112, 193104 **(2018).**

[15] P. Xu, T. C. Droubay, J. S. Jeong, K. A. Mkhoyan, P. V. Sushko, S. A. Chambers, and B. Jalan, *Adv. Mater. Interfaces* 3, 1500432 **(2016).**

[16] P. Xu, Y. Ayino, C. Cheng, V. S. Pribiag, R. B. Comes, P. V. Sushko, S. A. Chambers, and B. Jalan, *Phys. Rev. Lett*. 117, 106803 **(2016).**

[17] S. A. Chambers, L. Qiao, T. C. Droubay, T. C. Kaspar, B. W. Arey, and P. Sushko, *Phys. Rev. Lett.* 107, 206802 **(2011).**

[18] R. B. Comes, S. R. Spurgeon, D. M. Kepaptsoglou, M. H. Engelhard, D. E. Perea, T. C. Kaspar, Q. M. Ramasse, P. V. Sushko, and S. A. Chambers, *Chem. Mater. 29*, 1147 **(2017).**

[19] A. Fête, C. Cancellieri, D. Li, D. Stornaiuolo, A. Caviglia, S. Gariglio, and J.-M. Triscone, *Appl. Phys. Lett.* 106, 051604 (**2015**).

[20] A. Kalabukhov, R. Gunnarsson, J. Börjesson, E. Olsson, T. Claeson, and D. Winkler, *Phys. Rev. B* 75, 121404 (**2007**).

[21] M. Kawasaki, K. Takahashi, T. Maeda, R. Tsuchiya, M. Shinohara, O. Ishiyama, T. Yonezawa, M. Yoshimoto, and H. Koinuma, *Science* 266, 1540 (**1994**).

[22] I. Robinson and D. Tweet, *Rep. Prog. Phys*. 55, 599 (**1992**).

[23] M. Björck and G. Andersson, *J. Appl. Crystallography*. 40, 1174 (**2007**).

[24] S. Koohfar, A. Disa, M. Marshall, F. Walker, C. Ahn, and D. Kumah, *Phys. Rev. B* 96, 024108 (**2017**).

[25] T. Chen, K. Ahmadi-Majlan, Z. H. Lim, Z. Zhang, J. H. Ngai, A. F. Kemper, and D. P. Kumah, *Appl. Phys. Lett.* 113, 201601 (**2018**).

[26] K. Maiti and D. Sarma, *Phys. Rev. B* 54, 7816 (**1996**).

[27] R. Colby, L. Qiao, K. Zhang, V. Shutthanandan, J. Ciston, B. Kabius, and S. A. Chambers, *Phys. Rev. B* 88, 155325 (**2013**).

[28] L. Qiao, T. C. Droubay, M. E. Bowden, V. Shutthanandan, T. C. Kaspar, and S. A. Chambers, *Appl. Phys. Lett.* 99, 061904 (**2011**).

[29] D. Marrocchelli, N. H. Perry, and S. R. Bishop, *Phys. Chem. Chem. Phys*. 17, 10028 (**2015**). [30] C. Cazorla, *Phys. Rev. Appl*. 7, 044025 (**2017**).

[31] K. Han et al., *Sci. Rep*. 6, 25455 (**2016**).

[32] H. Xue et al., *Phys. Rev. B* 98, 085305 (**2018**).

[33] S. Das, A. Rastogi, L. Wu, J.-C. Zheng, Z. Hossain, Y. Zhu, and R. Budhani, *Phys. Rev. B* 90, 081107 (**2014**).

[34] K. Zhang, Y. Du, P. Sushko, M. E. Bowden, V. Shutthanandan, S. Sallis, L. F. Piper, and S. A. Chambers, *Phys. Rev. B* 91, 155129 (**2015**).

[35] Y. Chen et al., *Nat. Commun*. 4, 1371 (**2013**).

[36] Q. Fu and T. Wagner, *Surf. Sci*. 601, 1339 (**2007**).

[37] Y. Chen, N. Pryds, J. E. Kleibeuker, G. Koster, J. Sun, E. Stamate, B. Shen, G. Rijnders, and S. Linderoth, *Nano Lett.* 11, 3774 (**2011**).

[38] Y. Li, S. N. Phattalung, S. Limpijumnong, J. Kim, and J. Yu, *Phys. Rev. B* 84, 245307 (**2011**). [39] Z. Liu et al., *Phys. Rev. X* 3, 021010 (**2013**).

[40] I. Weinberg and P. Larssen, *Nature* 192, 445 (**1961**).

[41] K. Ueda, H. Tabata, and T. Kawai, *Science* 280, 1064 (**1998**).

[42] J.-S. Zhou, J. Alonso, A. Muonz, M. Fernández-Díaz, and J. Goodenough, *Phys. Rev. Lett*. 106, 057201 (**2011**).

.

Chapter 4

Correlating polar distortions and interfacial charge at the polar/non-polar $LaCrO_3/SrTiO_3$ (001) interface

This chapter is based upon the following publication:

A. Al-Tawhid, D. P. Kumah, *AIP advances*, 10 (4), p. 045132. (2020).

Contributions:

The author grew the materials and performed the X-ray diffraction and structure analysis and the electrical transport measurement

4.1 Preface

The relationship between the sheet carrier concentration, ns, of $LaCrO_3$(LCO)/$SrTiO_3$(STO) heterostructures and their structural properties has been investigated. Under low oxygen partial pressure, the STO substrate is reduced during growth as evidenced by a high ns of 10^{16} cm^{-2}. By controlling the post-growth annealing conditions, heterostructures with ns of 10^{13}–10^{16} cm^{-2} are achieved. The atomic-scale structure of the samples is obtained using high-resolution synchrotron x-ray diffraction measurements. For heterostructures with ns at or below 3×10^{13} cm^{-2}, polar distortions are present within the LCO layers and increase in magnitude with a decrease in sheet carrier concentration. These distortions are absent for samples with ns on the order of 10^{15}–10^{16} cm^{-2} where interfacial carriers play a role in alleviating the polar discontinuity at the LCO/STO interface. These results suggest that interfacial charge carriers and polar distortions can act as complementary mechanisms to alleviate the polar discontinuity at polar/non-polar complex oxide interfaces.

4.2 Introduction

The discovery of emergent electronic and magnetic phenomena at polar/non-polar perovskite oxide interfaces not found in bulk has sparked considerable interest by the scientific community.[1–5] At such interfaces, the discontinuity in the charge stacking leads to a polar catastrophe characterized by the divergence of the electrostatic potential with an increase in the thickness of the polar material. Relaxation of the divergent potential leads to the emergence of functional properties including high-mobility two-dimensional conductivity and interfacial magnetism.6 Various mechanisms have been proposed to occur to alleviate the polar discontinuity including charge transfer,[1] intermixing,[7] cation and anion vacancies,[8,9] and ferroelectric-like structural distortions.[10–14]

In this Letter, we focus on the relationship between ionic structural relaxations that arise to screen the electric field within the polar layer and the interfacial charge density at the interface between (001)-oriented polar $LaCrO_3$(LCO) films and non-polar $SrTiO_3$(STO).[15–18] Along the [001] crystallographic direction, LCO may be viewed as alternating positively charged (LaO) + layers and negatively charged (CrO_2) − layers, while the STO substrate comprises alternating neutral (SrO) and (TiO_2) layers. Ferroelectric-like ionic rumpling within the LCO layers leads to a lattice polarization, which can reduce the electric field within the LCO film. The role of lattice distortions in mitigating the polar catastrophe has been studied theoretically and experimentally in the canonical polar $LaAlO_3$ (LAO)/non-polar STO system.[10–12,19–21] The lattice polarization within LAO is predicted to sufficiently reduce the electric field buildup to avoid triggering an electronic reconstruction in LAO films with thicknesses below 4–5 unit cells.[10] Using surface diffraction measurements, Pauli et al. investigated the lattice distortions in LAO films on STO as a function of the LAO thickness and found a decrease in the depolarizing buckling with LAO

thickness.[11] Above the critical thickness for metallicity, intrinsic (electronic reconstruction) and extrinsic (e.g., arising from oxygen vacancies) charge carriers at the interface can provide additional screening of the electric field within the polar film. A critical question we seek to address is the relative roles of lattice (polar distortions), chemical interactions (oxygen vacancies), and electronic reconstructions (charge transfer) in ameliorating the polar discontinuity at polar/non-polar oxide interfaces. Here, we perform a systematic study of the LCO/STO interfacial carrier concentration that can be tuned by growth and post-growth conditions and their relation to the lattice polarization to develop a comprehensive understanding of the unique physical properties that emerge at polar/non-polar interfaces.

The structural and electronic properties of antiferromagnetic LCO films on single crystal Ti-terminated STO are investigated using a combination of high-resolution synchrotron x-ray diffraction measurements with structural refinement methods and magnetoresistance (MR) measurements. Conducting two-dimensional LCO/STO interfaces are achieved by a systematic control of synthesis conditions.[15,22,23] LCO films are grown by molecular beam epitaxy (MBE) under conditions that reduce the LCO film and the STO substrate.[15] By controlling the post-growth annealing conditions, the sheet carrier concentration of the system can be systematically tuned from 10^{16} cm^{-2}, indicative of bulk conduction within the substrate, to 10^{13} cm^{-2}, indicative of quasi-two dimensional conductivity at the LCO/STO interface. The dimensionality is confirmed by in-plane MR measurements. The atomic-scale structure of the LCO/STO interface is determined as a function of the measured sheet carrier concentration. For sheet carrier concentrations (ns) greater than 10^{15} cm^{-2}, no polar distortions are observed within the LCO films, suggesting that there are enough interfacial carriers to alleviate the polar discontinuity. As ns is decreased by annealing in oxygen, polar distortions emerge within the LCO film. The magnitude

of the polar distortions, characterized by cation-oxygen rumpling along the growth direction, is found to be inversely proportional to the sheet carrier concentration (n_s). These results suggest an interplay between polar distortions and interfacial charge in mitigating the polar discontinuity at polar/non-polar oxide interfaces.

4.3 Experimental Methods

4.3.1 Growth and treatment

LCO films were grown on (001)-oriented STO substrates using oxygen-assisted molecular beam epitaxy (MBE). Prior to growth, the STO substrates were treated with buffered HF and annealed in flowing oxygen at 1100 °C in a tube furnace for 2 h to create a Ti-terminated surface.[24] The LCO films were grown at 850 °C and at 1×10^{-7} Torr oxygen partial pressure. The La and Cr fluxes were calibrated prior to growth with a quartz crystal microbalance. Samples of nominally 10-unit cell (uc) LCO were grown, and reflection high energy electron diffraction (RHEED) was used to monitor the film thickness and crystallinity during growth. After growth, the oxygen was turned off and the samples were cooled to room temperature in vacuum. Samples were annealed ex-situ in a tube furnace in 1 atm flowing oxygen at 250 °C for 2 h, 300 °C for 2 h, and 350 °C for 4 h to control the effective sheet carrier concentrations.

Table 4.1. Summary of samples with different post-growth anneal conditions and their respective measured carrier concentrations, ns.

Sample	A	B	C	D
Annealing conditions	Unannealed	2 hours 250 ^{o}C	2 hours 300 ^{o}C	4 hours 350 ^{o}C
n_s (cm^{-2})	2 x 10^{16}	2 x 10^{15}	3 x 10^{13}	1 x 10^{13}

4.3.2 Transport

Electrical measurements were carried out in the van der Pauw configuration in the temperature range of 10–300 K. Gold contacts were deposited on the corners and aluminum wires were ultrasonically bonded to the contacts for sheet resistance and Hall measurements. In-plane magnetoresistance (MR) measurements were performed in a range of −4 T to 4 T. All measurements were carried out in a Quantum Design physical property measurement system (PPMS).

4.3.3 X-ray diffraction measurements

To determine the atomic-scale structures of the samples as a function of the carrier concentration, crystal truncation rods (CTR) along seven symmetry-inequivalent STO crystallographic directions were obtained with an x-ray energy of 16 keV at room temperature. The diffraction measurements were performed at beamline 33ID at the Advanced Photon Source.

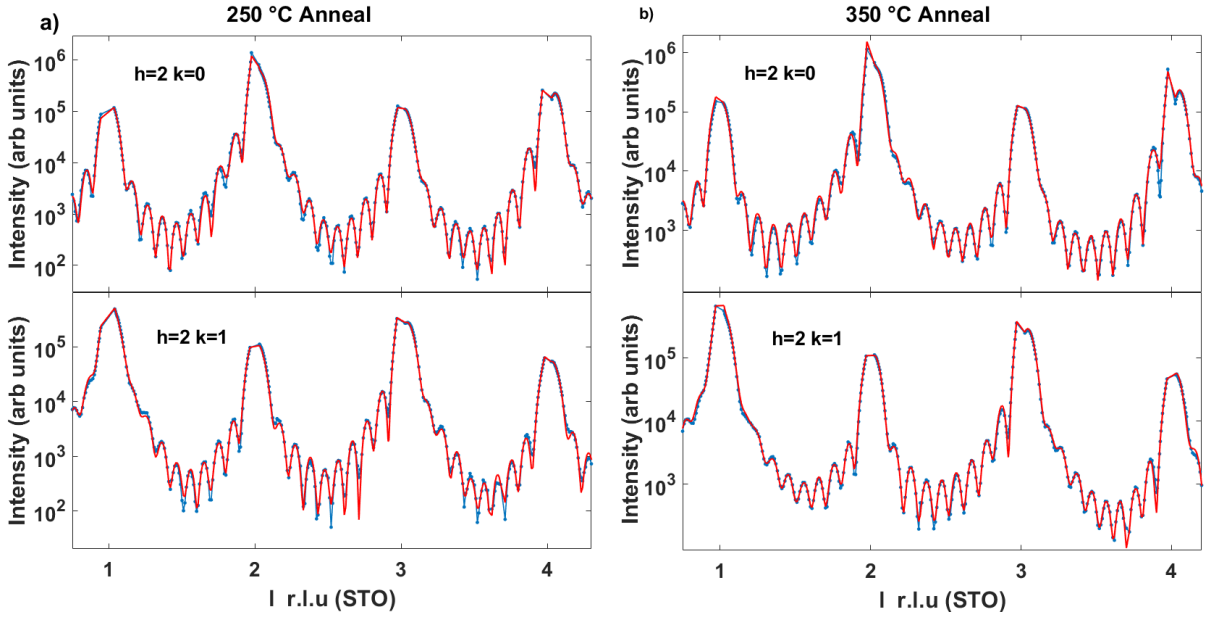

Figure 4.1. The (2 0 L) and (2 1 L) crystal truncation rod (CTR) for the LCO/STO heterostructures which were annealed a) at 250^{o}C for 2 hours (Sample B) and b) at 350^{o}C for 4 hours (Sample D).The blue circles represent the measured values and the red curves are the fit. The Miller indicesh, k and l are in units of the bulk STO reciprocal lattice vectors (1 r.l.u.= 1/3.905 ˚A^{-1}).

The atomic-scale structure of the films was determined from fitting the measured CTRs using a genetic-based fitting algorithm GenX.[25] The parameters of the fits were the out-of-plane lattice constant for each atomic layer in the film and the first five layers of the substrate, the chemical composition of the first five layers of the film and substrate to account for intermixing, and the occupations of the topmost two layers of the film to account for roughness and their partial occupation. Additionally, all ions were allowed to displace in the z direction from their ideal high-symmetry positions and the oxygen octahedra were allowed to rotate and tilt. The converged structures were obtained by first minimizing the crystallographic R1 error function followed by a minimization of the LogR1 error function, where Imeasi and Icalci are the measured and

calculated intensity for the ith reflection. Representative CTRs along the [2 0 L] and [2 1 L] directions for the samples annealed at 250 (Sample B) and 350 ℃ (Sample D) and their fits are shown in Fig. 1, which show that the data and the converged structural models are in excellent agreement.

4.4 Results and discussion

An electronic reconstruction to remove the polar catastrophe is predicted to lead to the transfer of 0.5 electrons per unit cell from the LCO surface to the LCO/STO interface, leading to a ns of 3.3×10^{14} cm^{-2}.[26] For the as-grown LCO/STO (sample A), the measured ns is 2×10^{16} cm^{-2}. In-plane MR measurements for sample A are shown in Fig. 4.2. The MR for this sample is positive and linear indicative of 3D conduction within the bulk STO substrate due to oxygen vacancies.[27,28] Annealing in 1 atm of flowing oxygen at 250 °C, 300 °C, and 350 ℃ results in a ns of 2×10^{15} (sample B), 3×10^{13} (sample C), and 1×10^{13} cm^{-2} (sample D), respectively. Further annealing of the 350 ° C sample at higher temperatures or for longer time leads to no observable change in the transport properties. Table I summarizes the annealing conditions and the measured carrier concentrations.

The in-plane MR measurements at 10 K for the annealed samples are compared in Fig. 4.2 as a function of ns. For sample B, the MR is positive and suppressed relative to the as-grown sample indicative of a proximity to a 3D-2D transition.

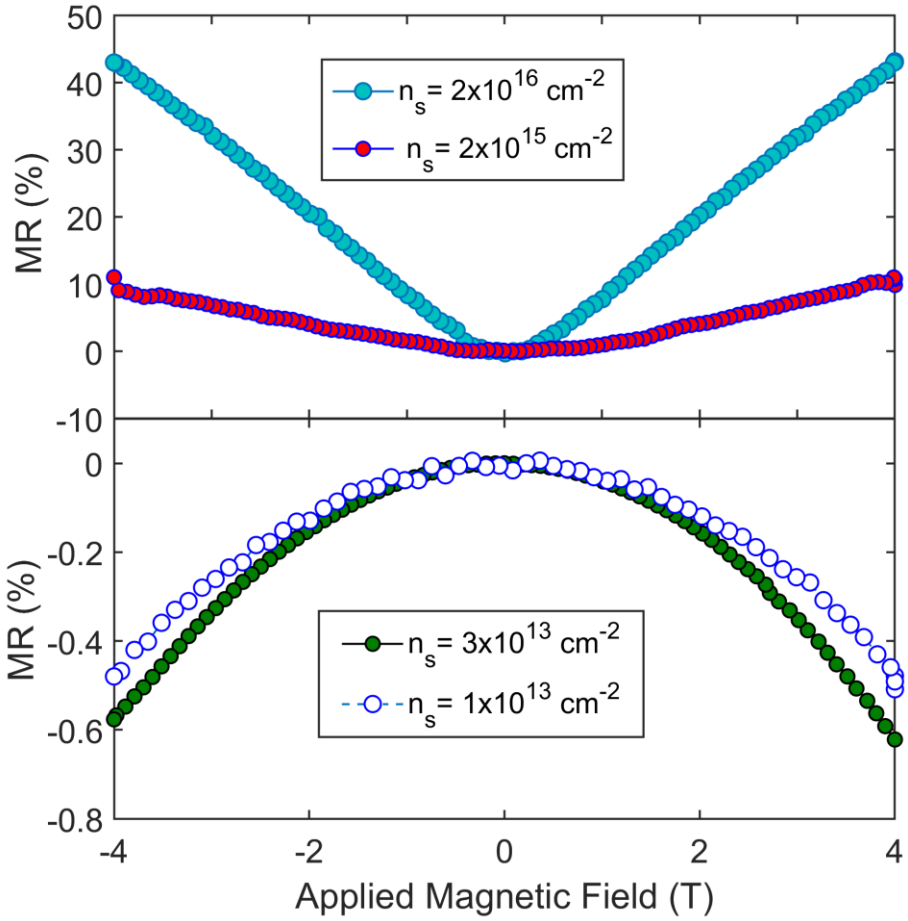

Figure 4.2. In-plane magnetoresistance of the 10 uc LCO/STO heterostructures as a function of the measured sheet carrier concentrations at 10 K. The carrier concentrations are dependent on the post-growth annealing conditions.

The measured ns of 3×10^{13} cm^{-2} and 1×10^{13} cm^{-2} for samples C and D, respectively, are more than an order of magnitude smaller than the theoretical expected value of 3.3×10^{14} cm^{-2} required to alleviate the polar discontinuity. However, these values are in agreement with reports for the two-dimensional electron gas (2DEG) formed at the LAO/STO interface where ns is on the order of 1×10^{13} cm^{-2} for fully oxidized samples.8 The in-plane MR for samples C and D is quadratic and negative and characteristic of carriers confined to two-dimensions.

A possible consequence of the decreased carrier concentration is the inability of the interfacial carriers to completely mitigate the electrostatic potential built up within the LCO film, leading to cation–anion buckling within the polar film.[11,20] Thus, to determine the effect of the sheet carrier concentration on the structural properties of the LCO layers, we compare the atomic-scale structures determined from fits to the measured crystal truncation rods. The fraction of the terminating layer of the film coherently strained to STO was less than 20% due to surface roughness and/or surface disorder induced by the annealing process.[29] Hence, the structural results for the terminating LCO layers are excluded from the analysis below due to the large uncertainty in determining the atomic coordinates for this layer. Figure 3 shows the layer-resolved the LCO film (layer >0). The STO layers from layer 5 to layer 2 have lattice parameters of 3.905 Å, as expected for bulk STO. The topmost two STO layers are expanded to 3.95–3.98 Å. This expansion has been previously attributed to the presence of Ti3+ due to the charge transfer from the film surface and/or La/Sr intermixing across the interface. [7,30]

Within the LCO film, there is a decay in the LCO lattice constant from 3.93 ± 0.01 Å in the first LCO layer to 3.87 ± 0.01 Å below the film surface, which is close to the bulk pseudo cubic lattice constant of 3.88 Å.[29] An expansion of the surface LCO layer is observed for the three films. Except for the topmost layer, the identical lattice spacings for the films with different carrier concentrations are indicative of identical oxygen stoichiometry within the LCO layers. The anomalous expansion of the surface layers of the LCO films is likely due to a higher concentration of oxygen vacancies induced by the polar field. [23,31]

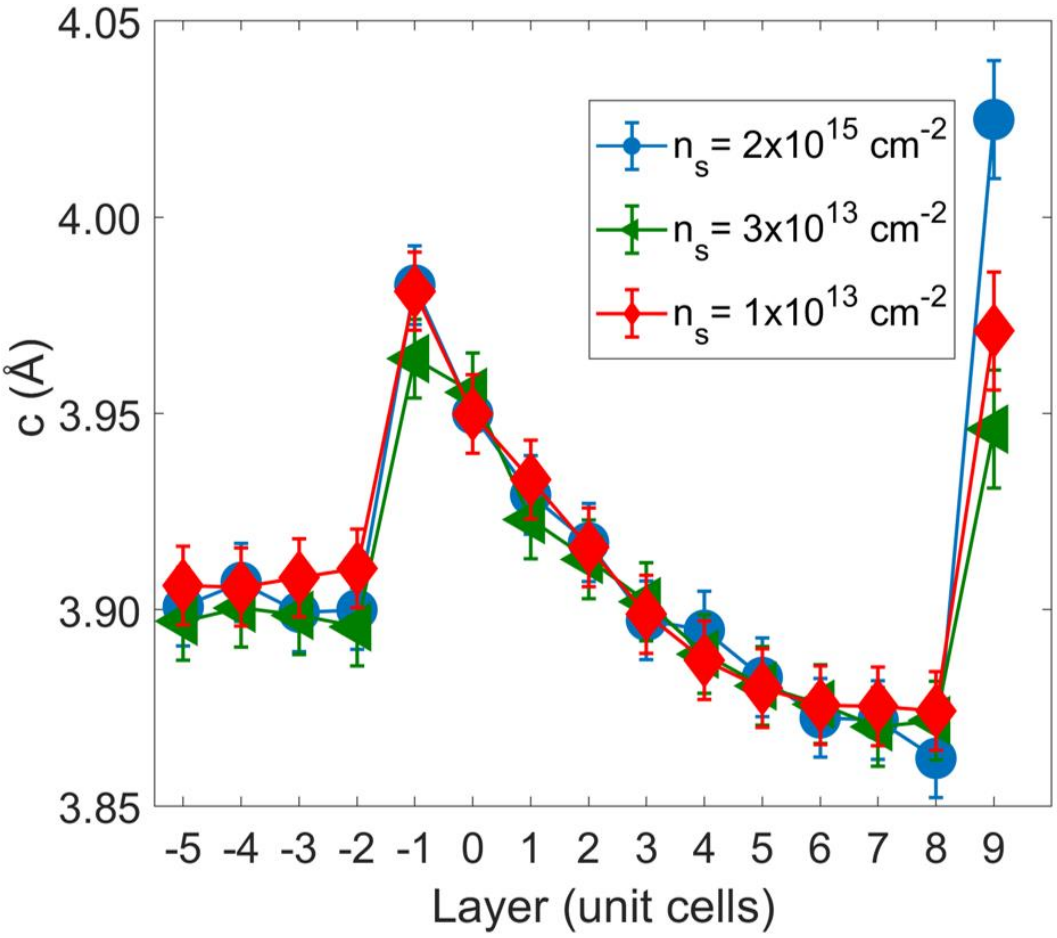

Figure 4.3. Layer resolved out-of-place lattice constant, c, for LCO/STO heterostructures of various sheet carrier concentrations ns. Layer 1 indicates the first LCO layer.

Within each LCO layer, we determine the polar displacement along the [001] direction between the cation and ions in Fig. 4.4 as a function of ns. For the sample with ns = 2×10^{15} cm^{-2}, no polar rumpling is observed within the LCO film. The absence of polar distortions in the LCO indicates that the interfacial charge completely mitigates the polar discontinuity.

For samples with ns below the minimum value needed to completely compensate the polar discontinuity, polar distortions are present in the LCO film (Fig. 4) increasing linearly from the LCO/STO interface to the LCO surface. [11,12,20,32]

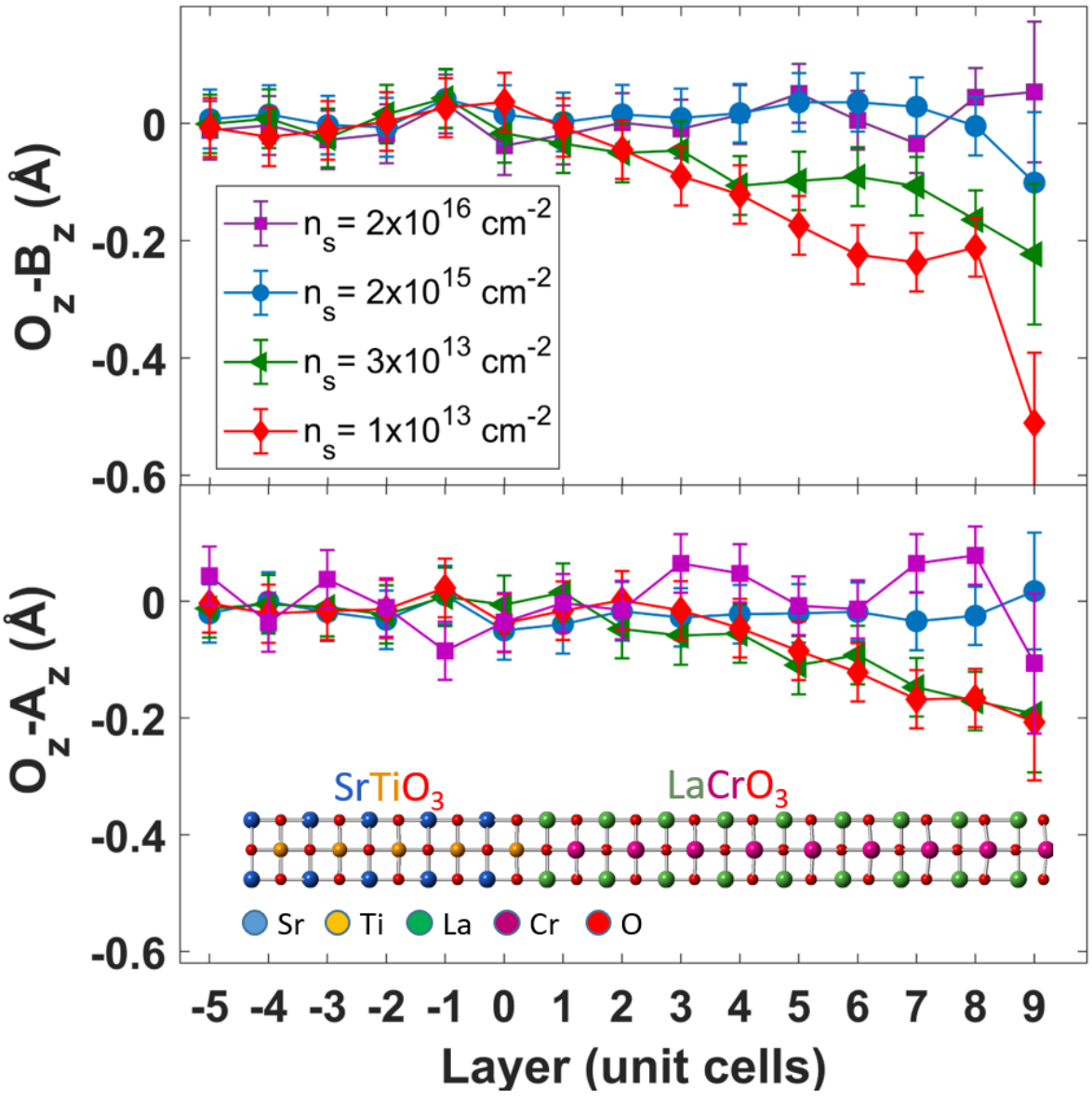

Figure 4.4. Polar distortions in the B(Ti,Cr)O_2(top panel) and A(Sr,La)O planes (lower panel) as a function of layer. Positive values indicate displacement of the oxygen anions towards the film surface relative to the cation positions. The inset shows the atomic structure for the LCO/STO sample with ns= $1\times10^{13}cm^{-2}$

The occurrence of polar distortions in samples C and D is consistent with surface diffraction [11,19] and electron microscopy measurements[13] on the LAO/STO system where a polarization is found within the LAO film above the critical LAO film thickness for metallicity, tc. Additionally, we do not observe a significant polarization within the interfacial STO layers at the LCO/STO interface or a collapse of the displacements in the LaO planes. [11,13,19]

The decrease in ns upon annealing and the subsequent formation of polar distortions suggest that the origin of the 2DEG is at least partially dependent on oxygen vacancies. A possible mechanism for the 2DEG formation is an oxygen vacancy mediated electronic reconstruction.[31] An illustration of the process is shown in Fig. 5. Here, oxygen vacancies Vo form at the polar LCO surface in response to the diverging electrostatic potential. [31,33] The ionization of the surface defects leads to electronic transfer to the interface to cancel the polar field induced by the polar discontinuity.

We conclude from the relationship between the structural polar distortions and the post-growth anneal conditions in Fig. 4.3 that as the surface oxygen vacancy concentration is decreased by annealing, less charge is donated to the interface. This results in a decrease in ns and an incomplete screening of the polar field. To compensate the remaining field, polar distortions in the form of buckling of the LaO and CrO_2 planes occur to help mitigate the electrostatic buildup. Thus, the polar discontinuity is mitigated by a combination of electronic transfer and polar distortions.

In the case of insulating LCO/STO interfaces that can be achieved by lower growth temperatures or higher growth oxygen partial pressures, a significant decrease in the lattice parameter has been observed compared to metallic samples. [15,23] Li et al.[23] proposed that a lattice expansion of LCO resulting from oxygen vacancies can decrease the ionic potential well depth in

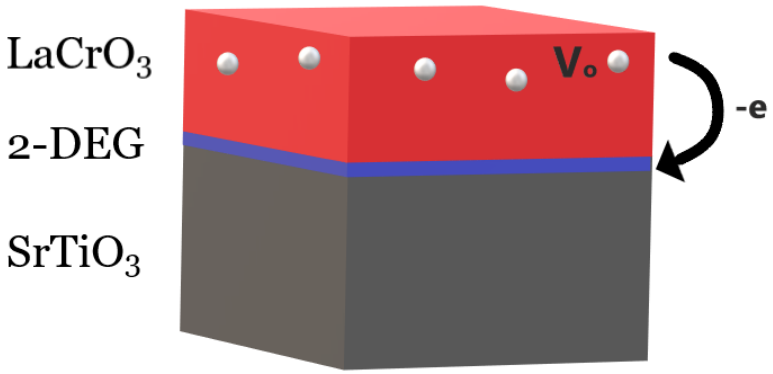

Figure 4.5. Illustration of mechanism for the formation of a 2D electron gas at the LCO/STO interface. Oxygen vacancies at the LCO surface donate electrons to the interface leading to the formation of a 2D electron gas on the STO side of the interface. Annealing in oxygen reduces the surface oxygen vacancy concentration and the available charge transferred to the interface.

the LCO to facilitate charge transfer to the interface. Since no significant changes in the lattice constants of the films are observed on annealing except for the surface, we conclude that the interface potential well depth and the concentration of out-diffused Ti in the LCO film[17] are unaffected by the anneal and the main changes on annealing are the surface oxygen vacancy concentration.

4.5 Conclusion

In summary, we have shown that polar distortions and interfacial charge play complementary roles in relieving the polar discontinuity at the polar/non-polar LCO/STO interface. By controlling the post-growth annealing procedure, heterostructures with sheet carrier concentrations of 2×10^{15} cm^{-2} to 1×10^{13} cm−2 are achieved. Heterostructures with a sheet carrier concentration of 2×10^{15} cm^{-2} and higher exhibit large positive linear in-plane MR at 10 K, while samples with 3×10^{13} cm^{-2} or lower exhibit negative and quadratic in-plane MR indicative of 2D conduction.

The growth and annealing conditions lead to different structural ground states of the polar film. We observe a strong correlation between the polar distortions within the LCO films and the carrier concentration. Polar distortions in the form of buckling of A–O and B–O_2 planes form when the sheet carrier concentration is on the order of 1×10^{13} cm^{-2}. The absence of structural distortions in samples with ns on the order of 10^{15}–10^{16} cm^{-2} indicates that interfacial carriers are sufficient to mitigate the polar discontinuity. For most perovskite complex oxides including LCO, the physical properties including magnetism are coupled to the transition metal–oxygen bond. The effect of the induced polar distortions on antiferromagnetic ordering is of particular interest due to the potential coupling of magnetic ordering in the polar LCO film with charge carriers within the confined electron gas.

REFERENCES

[1] A. Ohtomo and H. Hwang, *Nature* 427, 423 (**2004**)

[2] A. Brinkman, M. Huijben, M. van Zalk, J. Huijben, U. Zeitler, J. Maan, W. G. van der Wiel, G. Rijnders, D. H. Blank, and H. Hilgenkamp, *Nat. Mater.* 6, 493 (**2007**).

[3] F. J. Wong, S.-H. Baek, R. V. Chopdekar, V. V. Mehta, H.-W. Jang, C.-B. Eom, and Y. Suzuki, *Phys. Rev. B* 81, 161101 (**2010**).

[4] J. Mannhart and D. Schlom, *Science* 327, 1607 (**2010**).

[5] N. Reyren, S. Thiel, A. D. Caviglia, L. Fitting Kourkoutis, G. Hammerl, C. Richter, C. W. Schneider, T. Kopp, A.-S. Rüetschi, D. Jaccard, M. Gabay, D. A. Muller, J.-M. Triscone, and J. Mannhart, *Science* 317, 1196 (**2007**).

[6] J. A. Bert, B. Kalisky, C. Bell, M. Kim, Y. Hikita, H. Y. Hwang, and K. A. Moler, *Nat. Phys***.** 7, 767 (**2011**).

[7] P. Willmott, S. Pauli, R. Herger, C. Schlepütz, D. Martoccia, B. Patterson, B. Delley, R. Clarke, D. Kumah, C. Cionca et al., *Phys. Rev. Lett*. 99, 155502 (**2007**).

[8] A. Kalabukhov, R. Gunnarsson, J. Börjesson, E. Olsson, T. Claeson, and D. Winkler, *Phys. Rev. B* 75, 121404 (**2007**).

[9] Z. Liu, C. Li, W. Lü, X. Huang, Z. Huang, S. Zeng, X. Qiu, L. Huang, A. Annadi, J. Chen et al., *Phys. Rev. X* 3, 021010 (**2013**).

[10] R. Pentcheva and W. E. Pickett, *Phys. Rev. Lett*. 102, 107602 (**2009**).

[11] S. Pauli, S. Leake, B. Delley, M. Björck, C. W. Schneider, C. Schlepütz, D. Martoccia, S. Paetel, J. Mannhart, and P. Willmott, *Phys. Rev. Lett*. 106, 036101 (**2011**).

[12] M. Salluzzo, S. Gariglio, X. Torrelles, Z. Ristic, R. Di Capua, J. Drnec, M. M. Sala, G. Ghiringhelli, R. Felici, and N. Brookes, *Adv. Mater*. 25, 2333 (**2013**).

[13] P. Lee, V. Singh, G. Guo, H.-J. Liu, J.-C. Lin, Y.-H. Chu, C. Chen, and M.-W. Chu, *Nat. Commun.* 7, 12773 (**2016**).

[14] Y. Segal, J. Ngai, J. Reiner, F. Walker, and C. Ahn, *Phys. Rev. B* 80, 241107 (**2009**).,

[15] A. Al-Tawhid, J. R. Frick, D. B. Dougherty, and D. P. Kumah, *J. Vac. Sci. Technol., A* 37, 021102 (**2019**).

[16] R. B. Comes, S. R. Spurgeon, D. M. Kepaptsoglou, M. H. Engelhard, D. E. Perea, T. C. Kaspar, Q. M. Ramasse, P. V. Sushko, and S. A. Chambers, *Chem. Mater*. 29, 1147 (**2017**).

[17] S. A. Chambers, L. Qiao, T. C. Droubay, T. C. Kaspar, B. W. Arey, and P. Sushko, *Phys. Rev. Lett*. 107, 206802 (**2011**).

[18] S.-C. Lin, C.-T. Kuo, R. B. Comes, J. E. Rault, J.-P. Rueff, S. Nemšák, A. Taleb, J. B. Kortright, J. Meyer-Ilse, E. Gullikson et al., *Phys. Rev. B* 98, 165124 (**2018**).

[19] R. Yamamoto, C. Bell, Y. Hikita, H. Y. Hwang, H. Nakamura, T. Kimura, and Y. Wakabayashi, *Phys. Rev. Lett*. 107, 036104 (**2011**).

[20] R. Pentcheva and W. E. Pickett, *J. Phys.: Condens. Matter 22*, 043001 (**2010**).

[21] C. Cantoni, J. Gazquez, F. Miletto Granozio, M. P. Oxley, M. Varela, A. R. Lupini, S. J. Pennycook, C. Aruta, U. S. di Uccio, P. Perna et al., *Adv. Mater*. 24, 3952 (**2012**).

[22] Y.-P. Hong, X.-X. Wang, G.-L. Qu, C.-J. Li, H.-X. Xue, K.-J. Liu, Y.-C. Li, C.-M. Xiong, R.-F. Dou, L. He et al., *Chin. Phys. B* 27, 047301 (**2018**).

[23] C.-J. Li, H.-X. Xue, G.-L. Qu, S.-C. Shen, Y.-P. Hong, X.-X. Wang, M.-r. Liu, W.-m. Jiang, P. Badica, L. He et al., *Sci. Rep*. 8, 195 (**2018**).

[24] M. Kawasaki, K. Takahashi, T. Maeda, R. Tsuchiya, M. Shinohara, O. Ishiyama, T. Yonezawa, M. Yoshimoto, and H. Koinuma, *Science* 266, 1540 (**1994**).

[25] M. Björck and G. Andersson, *J. Appl. Crystallogr*. 40, 1174 (**2007**).

[26] J. Lee and A. A. Demkov, *Phys. Rev. B* 78, 193104 (**2008**).

[27] M. Basletic, J.-L. Maurice, C. Carrétéro, G. Herranz, O. Copie, M. Bibes, É. Jacquet, K. Bouzehouane, S. Fusil, and A. Barthélémy, *Nat. Mater*. 7, 621 (**2008**).

[28] X. Wang, W. Lü, A. Annadi, Z. Liu, K. Gopinadhan, S. Dhar, T. Venkatesan et al., *Phys. Rev. B* 84, 075312 (**2011**).

[29] L. Qiao, T. C. Droubay, M. E. Bowden, V. Shutthanandan, T. C. Kaspar, and S. A. Chambers, *Appl. Phys. Lett*. 99, 061904 (**2011**).

[30] S. A. Chambers, M. H. Engelhard, V. Shutthanandan, Z. Zhu, T. C. Droubay, L. Qiao, P. Sushko, T. Feng, H. D. Lee, T. Gustafsson et al., *Surf. Sci. Rep*. 65, 317 (**2010**).

[31] L. Yu and A. Zunger, *Nature Commun*. 5, 5118 (**2014**).

[32] G. Singh-Bhalla, C. Bell, J. Ravichandran, W. Siemons, Y. Hikita, S. Salahuddin, A. F. Hebard, H. Y. Hwang, and R. Ramesh, *Nat. Phys*. 7, 80 (**2011**).

[33] M. Zhang, Z. Chen, B. Mao, Q. Li, H. Bo, T. Ren, P. He, Z. Liu, and Y. Xie, *Phys. Rev. Mater*. 2, 065002 (**2018**).

Chapter 5

Charge transfer and magnetism at $LaCrO_3/LaMnO_3$ superlattices grown on $SrTiO_3$

5.1 Preface

Polar $LaCrO_3/LaMnO_3$ (LCO/LMO) 2/2 superlattices are grown on (001) $SrTiO_3$ (STO). The mechanisms which this system compensates the polar discontinuity is studied and compared to the LCO/STO heterostructure. In the LCO/STO system one of the main mechanisms to alleviate the polar discontinuity is charge transfer from the top of LCO film to the STO resulting in the formation of a 2-dimensional electron gas. Inserting LMO layer in the form of a superlattice leads to charge accumulation in the LMO layers and an insulating interface between the first LCO and STO substrate. Additionally, the introduction of the LMO layers induces magnetism in our film via superexchange mechanism between Cr and Mn atoms. Squid and X-ray magnetic circular dichroism reveal that the superlattice is ferrimagnetic with the Cr anti-aligned with the Mn and applied field.

5.2 Introduction

Heterostructures of complex oxide perovskites have attracted considerable scientific interest since the discovery of novel properties at their interfaces that are not found in their bulk [1-4]. One of the more studied phenomena at oxide interfaces is the formation of a 2-dimensional electron gas (2-deg). The $LaAlO_3/SrTiO_3$ interface being the most studied and it believed to be the result of charge transfer due to the polar discontinuity [1]. Since its discovery, there have been numerous attempts to modify or improves the properties of the 2-deg at these interfaces. Some efforts have been made to improve the mobility of the 2-deg at both high and low temperatures [6]. Others have also attempted to modify the carrier concentration and even induce new magnetic properties [7]. The formation of a high mobility spin polarized 2-deg is would be major milestone in the spintronic field and would have many applications in the next generation of spintronic devices. Previous attempts have tried growing a magnetic overlayer on STO to induce magnetism via the magnetic proximity effect [8,9]. An example would be the case of $LaMnO_3$ (LMO) grown on STO. LMO is polar in the 001 direction and should result in charge transfer to mediate the polar discontinuity. However no 2-deg has yet to be shown to form at the interface. Instead, at some critical thickness of the LMO, ferromagnetism occurs [9], and it is thought to be the result of charge transfer from the top of the LMO to the LMO side of the interface [10]. While this does result in appearance of magnetism it suppressed the formation of a 2-deg since that charge does not make it to the STO. Other method that has been utilized to magnetize the 2-deg is the growth of a thin magnetic material in-between a heterostructure where a 2-deg is known to form. An example of this is the growth of LSMO thin films between LAO on STO[9]. However, an issue with this method is that when the magnetic material is grown to thick, the 2-deg disappears. On the other hand, growing a very thin film (<=1uc) results in the magnetic film losing its magnetic

properties due to the magnetic dead layer effect [11]. In this chapter we will attempt to grow superlattices of $LaCrO_3$/$LaMnO_3$ on STO. In the previous chapters we have shown that a 2-deg can form at the interface of LCO/STO and its properties can be tuning by controlling its growth and post growth conditions. By inserting LMO layers into the heterostructure, we can induce magnetism and study how charge transfer occurs in this mixed transition metal system.

5.3 Experimental methods

5.3.1 MBE growth

A 2-2 superlattice of LCO/LMO were grown on (001) STO using molecular beam epitaxy. The STO was treated prior to growth with and HF etch and annealed at 1000 ^{o}C for 2 hours to achieve a flat single terminated interface. 3 repeats of the superlattice were grown in total and a capping layer of 2uc LCO was grown on top. The sources were calibrated prior to growth using a quartz crystal microbalance. The samples were grown at 850 ^{o}C and in an oxygen partial pressure of $1.5x10^{-7}$Torr. After growth, samples were slowly cooled in $1x10^{-6}$ Torr of oxygen to eliminate oxygen vacancies present in the film and substrate.

5.3.2 Squid and XMCD

The magnetic properties were probed using a quantum design superconducting quantum interference device (SQUID). Measurements were carried out in the temperature range of 10 K to 300 K. The magnetic properties were also probed using X-ray magnetic circular dichroism (XMCD) measurements as the ALS at Berkeley.

5.3.2 Synchrotron X-ray Diffraction

Synchrotron X-ray diffraction measurements were performed at the 33ID beamline at the Advanced Photon Source. Crystal truncation rods (CTR's) [12] were measured using the bulk STO crystal lattice direction. The energy of the incident X-ray beam was 16 eV. The structure and composition were obtained from fitting multiple CTR's using a genetic based algorithm, GenX [13].

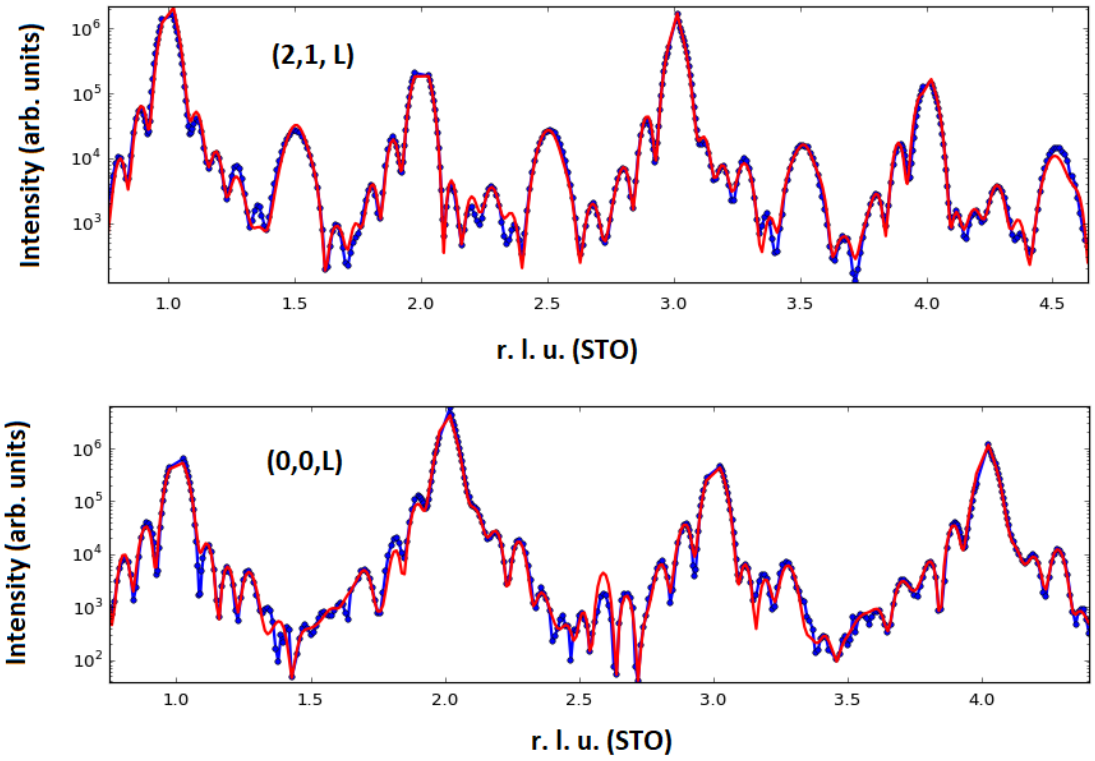

Figure 5.1. The (2 1 L) and (0 0 L) crystal truncation rod (CTR) for 3 repeats of LCO/LMO superlattice with 2uc LCO capping layer grown on (001) STO. The blue circles represent the measured values and the red curves are the fit. The Miller indices h, k, and l are in units of the bulk STO reciprocal lattice vectors (1 r.l.u.= 1/3.905 Å^{-1}).

The parameters fitted were the out-of-plane lattice constant for each layer, displacements of the atoms along the (001) direction and the oxygen octahedra's could rotate and tilt. The Debye-Waller factors were fitted, and each element was separated into three groups, the interface, the bulk and the surface to account for variations of the parameter in the film. The occupation of the top 3 layers were fitted to account for the roughness of the film surface. The CTR's and fit were compared to the data iteratively and the error between them was minimized.

5.4 Results and discussion

The structure of the LMO/LCO superlattice is shown in fig 5.2. Unlike the LCO/STO heterostructure there isn't a significant expansion at the interface followed by a gradual decrease in the out of plane lattice constant. Instead the lattice constant is relatively constant throughout the film. The presence of half order peaks in the off specular rods indicate that there is a doubling of the unit cells in the h and k direction. The absence of the half order peaks in the specular rod indicates that the doubling of the unit cell is not in the l direction. The intensity of the half order peaks can only be caused by displacements in the A site as the oxygen's rotations cannot produce those peaks with any realistic parameters. To elucidate the crystal structure and symmetry of our film, several half order rods are measured. The half order rods are much more sensitive to the rotations of the oxygen octahedra. While fitting of the half orders is more ambiguous due to the broad nature of the half order peaks, the absence and appearance of the peaks at certain position in reciprocal space can give a qualitative description of the symmetry of out film.

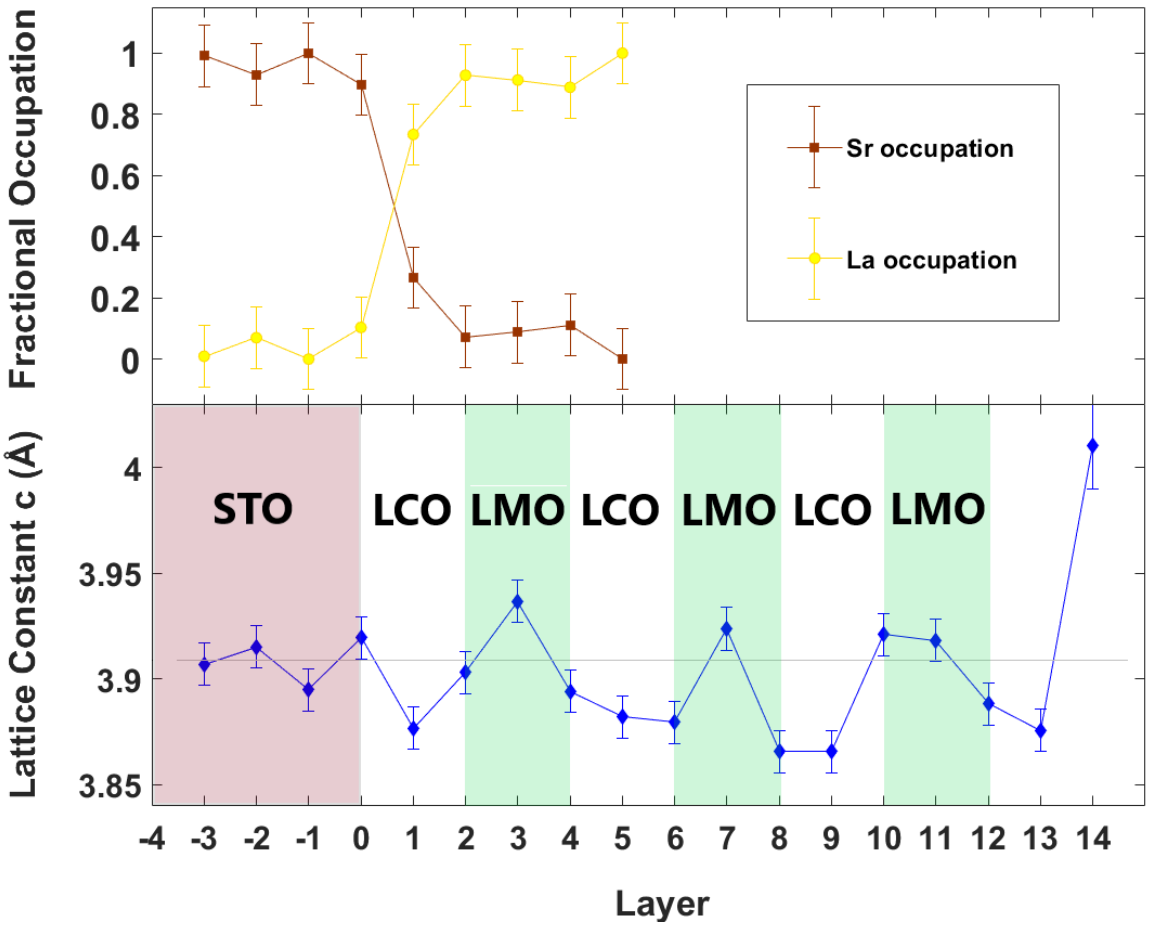

Figure 5.2. (Top) Layer-resolved Sr/La occupation for the LCO/LMO superlattice sample for the first 4 layers of the STO and the 5 first layers of the film. (Bottom) Layer-resolved out-of-plane lattice constant for the LCO/LMO sample. The grey horizontal line indicates the expected out of plane lattice constant for STO (3.905 Å). Color coding is to help distinguish the layers in the superlattice.

The presence of half order peaks along the (2 2 L) and (1/2, 0, L) rods indicate that our system exhibits an in-phase rotation along the in plane and out of plane direction. This lowering of the symmetry has an important effect on the magnetic properties of LMO [14] and could lead to a magnetic anisotropy of the system.

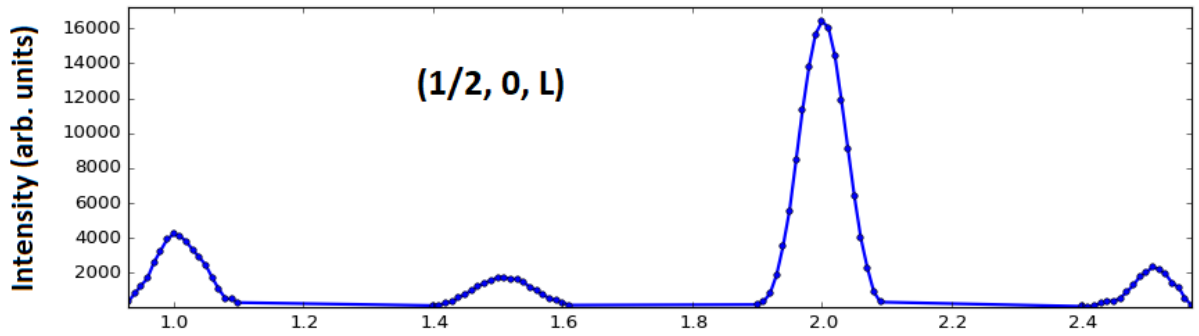

Figure 5.3. The (1/2 0 L) half order rod for 3 repeats of LCO/LMO superlattice with 2uc LCO capping layer grown on (001) STO. The blue circles represent the measured. The Miller indices h, k, and l are in units of the bulk STO reciprocal lattice vectors (1 r.l.u.= 1/3.905 Å^{-1}).

The addition of LMO layers in proximity to the LCO should result in a ferrimagnetic material [15]. The super exchange interaction between Mn^{+3} and Cr^{+3} is anti-ferromagnetic and since Mn^{+3} has a larger magnetic moment the result is a net magnetic moment. To confirm, the LCO/LMO superlattice's magnetic properties were measured using a Quantum Design SQUID system. Figure 2.a shows the magnetization as a function of field. The saturation magnetization is approximately 0.7 Bohr magnetons per Mn. The magnetization verses temperature graph in fig 5.3.b shows that the onset magnetization occurs at approximately 150K. The magnetization verses temperature was obtained after field cooling in a field of 5000 Oe. All measurements were performed with the magnetic field applied in-plane to the sample. The lower saturation magnetization is likely due to the Cr ion aligning anti-ferromagnetically to the Mn which reduces the net magnetic moment [11,15].

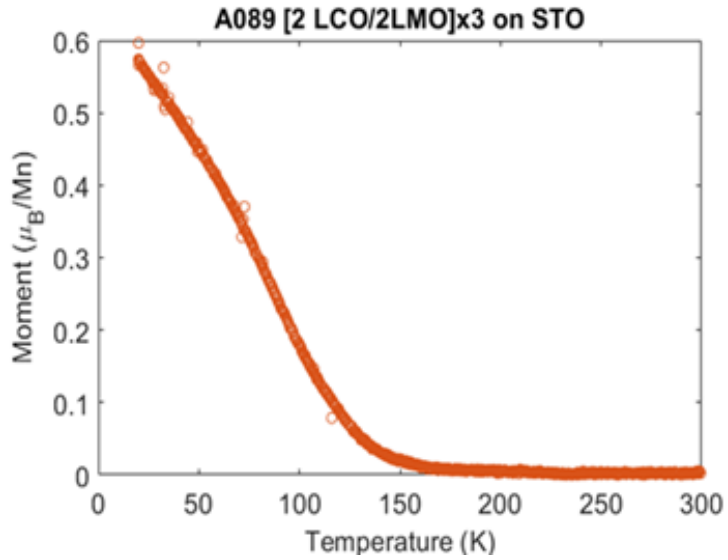

Figure 5.4. The magnetic moment vs temperature for our sample after field cooling in 5000 Oe field from 20K to 300K. The net moment is normalized to the number of Mn ions in our LMO layers. The onset of magnetism can be seen to be around 150K.

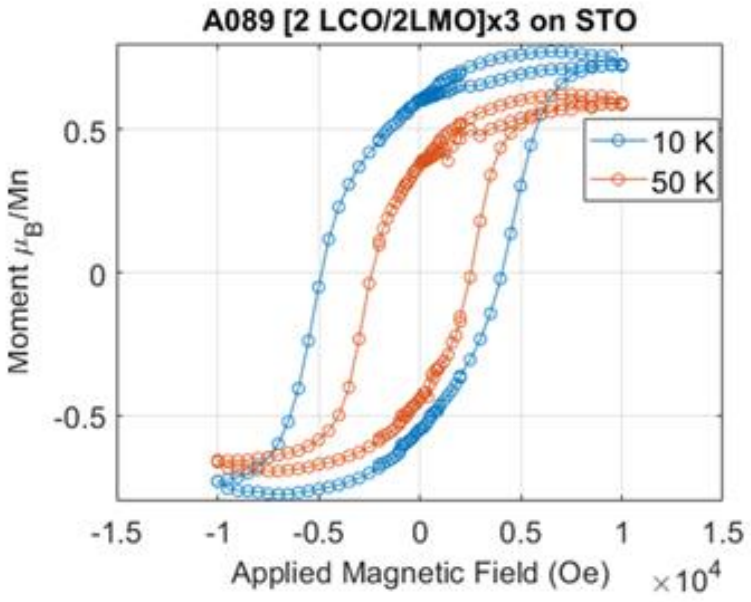

Figure 5.5. Hysteresis loop for our superlattice film at 10 K and 50 K. The coercivity field is quite large at approximately 5000 Oe at 10 K. The net moment is normalized to the number of Mn ions in our LMO layers.

To probe the element specific magnetism in our sample, we performed X-ray magnetic circular dichroism (XMCD) measurements at the Mn and Cr L-edges. The absorption of right and left circularly polarized light in total electron yield was performed in the presence of 0.5 Tesla magnetic field. The normalized intensity at the Mn and Cr edges are shown in the top half of figure 2. The difference between the difference between left and right circularly polarized light is shown in the bottom half of figure 2 and provide information about the magnetic properties of the Cr and Mn ions. From the absorption graphs we observe that the Cr is predominantly in the +3 state as expected. However, the Mn peaks show a large percent of +2 in addition to the expected +3. Clear magnetic dichroism is observed in the Mn ions confirming magnetism in the LMO layers.

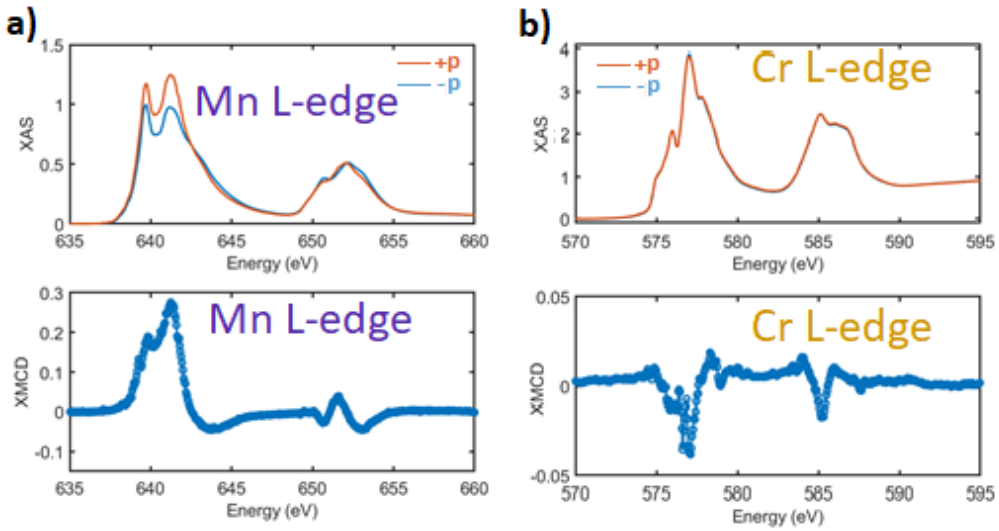

Figure 5.6. a) Normalized XAS of the superlattice at the Mn L-edge for positive and negatively circular polarized light. The difference XMCD signal showing the dichroism. b) Normalized XAS of the superlattice at the Cr L-edge for positive and negatively circular polarized light. The difference XMCD signal showing the dichroism but opposite of the Mn. Measurements were done at 10 K and in a field of 0.5 Tesla.

While the Cr exhibits a weaker dichroism, it also shows that the LCO is also magnetic. However, the dichroism is opposite to the Mn and the applied magnetic field direction. The weaker Cr dichroism could be a result of only the LCO unit cells that are adjacent to the LMO are ferromagnetic and anti-aligned to the LMO.

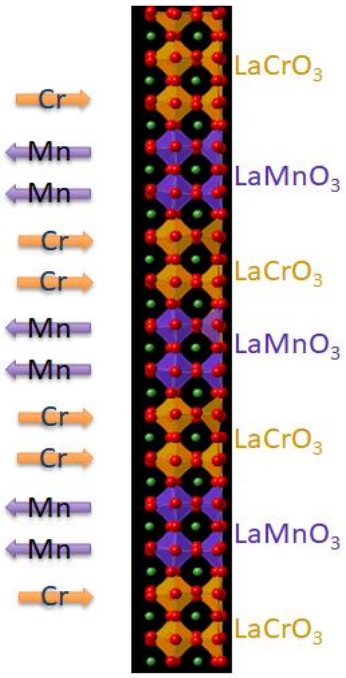

Figure 5.7. Illustration of the structure of the LCO/LMO superlattice with the magnetic moment of each layer. The LCO layer that are adjacent to the LMO are anti parallel to the LMO and reduce the net moment of the film.

Examining the electronic transport properties of our LCO/LMO superlattice on STO, we find that the heterostructure is insulating despite the film being polar and thick enough to trigger an electronic reconstruction [1,15]. While LCO grown on STO can form a 2deg at the interface under the corrected conditions [16,17], it has yet to be shown that a 2-deg can form at LMO/STO interface.

Instead at some critical thickness ferromagnetism occurs and it was thought that charge transfer occurs in these systems but is confined on the LMO side of the interface [4]. The result is a change in the Mn valence and ferromagnetism via the double exchange mechanism interface. However, the trapping of charges in the LMO side prevents the electron accumulation on the STO side and results in an insulating interface. It is possible that in our superlattice that charge transfer does occur but is trapped in our LMO layers. Indeed, the presence of a large percent of Mn^{+2} does support this hypothesis. Charge transfer from the top layer of LCO which is filled with V_o to the LMO layers would mediate the polar discontinuity but suppress the formation of a 2-deg.

5.5 Conclusion

In conclusion, we have grown 2/2 superlattices of LCO/LMO on STO (001). Synchrotron X-ray diffraction shows that the system is strained with good crystallinity. Examining the half order rods we determine that the film has two in phase rotations with a glazer notation of $a^+b^-c^+$. The superlattices are ferromagnetic as evidenced by the squid measurements with a Curies temperature of 150K. Elemental analysis of the magnetic properties using XMCD shows that the system is ferrimagnetic with some of the Cr atoms aligning opposite to the Mn atoms and the applied field. Despite the polar nature of the film, there is no measurable conductivity indicating that charge transfer to the substrate no longer occurs with the additions of the LMO layers. Instead, we believe that the charge transfer occurs from the top of the film to the LMO layers. This is supported by the large percent of Mn^{+2} in our LMO layers as evidence by the Mn-edge spectra. It is possible by controlling the thickness of the LCO and LMO layers and their positions that this charge transfer could be modulated leading to a different magnetic ground state of the system. Additionally, if the LMO layers are thin enough then it is possible that not enough charge

accumulates in the LMO layers and some will be transferred to STO leading to interfacial conductivity. Further work is necessary to elucidate how the mechanisms to alleviate the polar discontinuity evolves with changing the composition of the superlattice.

REFERENCES

[1] A. Ohtomo and H. Hwang, *Nature* 427, 423 (**2004**)

[2] A. Brinkman, M. Huijben, M. van Zalk, J. Huijben, U. Zeitler, J. Maan, W. G. van der Wiel, G. Rijnders, D. H. Blank, and H. Hilgenkamp, *Nat. Mater.* 6, 493 (**2007**).

[3] F. J. Wong, S.-H. Baek, R. V. Chopdekar, V. V. Mehta, H.-W. Jang, C.-B. Eom, and Y. Suzuki, *Phys. Rev. B* 81, 161101 (**2010**).

[4] J. Mannhart and D. Schlom, *Science* 327, 1607 (**2010**).

[6] Chen, Y., Bovet, N., Trier, F. et al. *Nat Commun,* **2013**, 4, 1371.

[7] Chen, Y. Z., et al, *Nature materials*, **2015** 14.8 801-806.

[8] Kormondy, Kristy J., et al., *Scientific reports*, 2018, 8.1 1-9.

[9] Wang, X. Renshaw, et al. *Science*, **2015** 716-719, 349.6249.

[10] Kaspar, Tiffany C., et al., *Advanced Materials Interfaces,* **2019**, 6.1, 1801428.

[11] S. Koohfar, et al. *Physical Review B,* **2017,** 96.2, 024108.

[12] I. Robinson and D. Tweet, *Rep. Prog. Phys*. 55, 599 (**1992**).

[13] M. Björck and G. Andersson, *J. Appl. Crystallography*. 40, 1174 (**2007**).

[14] Sanchez-Santolino, Gabriel, et al., *Microscopy and Microanalysis* 20.03 (**2014**).

[15] Deisenhofer, Joachim, et al. *Physical Review B,* 66.5 054414. **(2002).**

[16] A. Al-Tawhid, J. R. Frick, D. B. Dougherty, and D. P. Kumah, *J. Vac. Sci. Technol., A* 37, 021102 (**2019**).

[17] Y.-P. Hong, X.-X. Wang, G.-L. Qu, C.-J. Li, H.-X. Xue, K.-J. Liu, Y.-C. Li, C.-M. Xiong, R.-F. Dou, L. He et al., *Chin. Phys. B* 27, 047301 (**2018**).

Chapter 6

Conclusion and outlook

Complex oxide materials are a family of materials that host many exotic phenomena such as high temperature super conductivity, colossal magnetoresistance, and many forms of magnetism and ferroelectricity. The properties of these materials are often tried the strongly correlated nature of the d and f electrons they possess. Due to the narrow bandwidth and high spin orbit coupling of the d and f electrons, the properties of the material are very sensitive to distortions to the lattice and doping of the system. The application of strain can lead to a suppression of the magnetism of LSMO or a change of the magnetic ground state of LMO from antiferromagnetic to ferromagnetic. Doping of the Mott insulator LTO with oxygen or cation vacancies can cause the material to undergo an insulator to metal transition. While the properties of complex oxides are very exotic, the interface of two different complex oxide materials can sometimes lead to even more exotic properties not found in either material such as the formation of a 2-dimensional electron gas between LAO and STO. Understanding the origin of these properties and the mechanisms that can influence them is a necessary step to designing and fabricating the next generation of devices that utilize their exotic properties.

In this thesis we focused our attention on the interface of complex oxide polar materials grown on non-polar STO. At such interfaces, the polar discontinuity causes the electric potential to diverge and various mechanisms occur to mediate it. One mechanism is charge transfer, where electrons are transferred from the top of the polar film to the interface which can lead to the formation of a 2-dimensional electron gas. Since its discovery in 2004 by Ohtomo & Hwang at the interface of LAO/STO there have been many attempts to grow different polar oxide materials on STO. Many of these interfaces have also been shown to be conductive, but not all. The interface

between $LaCrO_3$, $LaMnO_3$, or $LaFeO_3$ and STO were first shown to be insulating. This was frustrating as studying the interplay between the high mobility 2-deg and these magnetic materials was a goal of the scientific community.

In this thesis we examine the LCO/STO interface in details and show that with careful control of the growth parameters and post growth treatment, the interface can be tuned from insulating to a high mobility 2-deg. Growing at higher temperature (800 vs 600 C) followed by a post anneal to remove oxygen vacancies in the STO reveals a 2-deg at the interface. Comparing the electron structure of the insulating to the metallic heterostructure using ARPES, we find that the LCO films are very similar. Using high resolution synchrotron X-ray diffraction and structural fitting we find that the LCO of the metallic heterostructure has a larger average out of plane lattice parameter than the insulating ones despite similar growth oxygen partial pressure and similar stoichiometry. The larger out of plane lattice constant is most likely due to a higher concentration of oxygen vacancies in out metallic concentration. These results highlight the importance of oxygen vacancies in the polar material in regard to the charge transfer mechanism to alleviate the polar discontinuity in the LCO/STO heterostructure.

Refining the structure of the metallic heterostructure even further we can examine the relationship between the amount of charge transfer and the structure. Annealing the metallic LCO/STO heterostructure with different temperatures and for different times we can achieve different sheet carrier concentrations as determined by hall data using the PPMS. Comparing the structure to the annealing time and temperature, we find that it does not have a significant effect on the lattice parameters. This suggests that while annealing does remove the oxygen vacancies in the STO it does not do the same in the LCO films to any significant degree. However, polar distortions begin to form in the LCO film when the sheet carrier concentration is below the 3.4e14

cm^{-2} that is theoretically needed to compensate the polar discontinuity. These results highlight how different mechanisms can occur to help mediate the polar discontinuity and offers another parameter when it comes to controlling the interface of complex oxide interfaces.

Lastly, we examined the effect of introducing LMO layers in LCO/STO heterostructure (in the form of an LCO/LMO superlattice) on the charge transfer mechanism. The goal of the LMO layers is to create an interface with a high mobility electron gas that is in proximity to a magnetic film. The goal is to spin polarized the 2-deg and achieve a system which combines both high mobility and a high degree of spin polarization. There is large interest in these types of systems in the design of spin transistors and logic devices combining the electronic and spin degree of freedom. Some of the strategy's researcher have employed are, inserting a very thin magnetic layer in between the polar material and STO, growing a magnetic film on STO and inducing a quasi-2-deg by leaching oxygen from the surface during growth, or growing STO film in between magnetic layers. Each of these strategies have led to some results, but to date there has been no experimental realization of a system which exhibit high mobility (>1000) and high degree of spin polarization. By introducing LMO layers into our LCO/STO in the form of an LCO/LMO superlattice, we induce magnetism in our polar material as evidence by squid and XMCD. However, we find that the formation of a 2-deg on the STO side is suppressed which we attribute to charge accumulation in the LMO layers.

While the realization of a high mobility spin polarized 2-deg at the LCO/LMO superlattice and STO was not achieved, there are still possibilities to explore. Growing thinner or less LMO layers will lead to less charge accumulation in those layers and possibly a return of the 2-deg. It may also be possible to prevent the charge accumulation by choosing a different material than LMO to induce magnetism which does not easily accommodate extra electrons.